Palaeogeography, Palaeoclimatology, Palaeoecology 629 (2023) 111779

Contents lists available at ScienceDirect

Palaeogeography, Palaeoclimatology, Palaeoecology

journal homepage: www.elsevier.com/locate/palaeo

Holocene relative sea-level changes on the southern east coast of the Yellow Sea

Dong-Yoon Yang [a], Min Han [a,*], Hyun Ho Yoon [a], Jin Cheul Kim [a], Eunseo Choi [b,**], Won-Jeong Shin [c], Jong-Yeon Kim [c], Arum Jung [a], Chanhyeok Park [d], Chang-Pyo Jun [e]

[a] Quaternary Environment Research Center, Korea Institute of Geoscience and Mineral Resources, 124 Gwahak-ro, Yuseong-gu, Daejeon 34132, Republic of Korea
[b] Center for Earthquake Research and Information, The University of Memphis, 3890 Central Ave, Memphis, TN 38152, USA
[c] Deparment of Geography Education, Chungbuk National University, 1, Chungdae-ro, Seowon-gu, Cheongju-si, Chungcheongbuk-do 28644, Republic of Korea
[d] Department of Astronomy, Space Science and Geology, Chungnam National University, Daejeon 34134, Republic of Korea
[e] Department of Earth Science Education, Chonnam National University, 77, Yongbong-ro, Buk-gu, Gwangju 61186, Republic of Korea

ARTICLE INFO

Editor: Prof. J. Yan

Keywords:
Holocene
Relative sea-level change
GIA model
Levering effect

ABSTRACT

Projections indicate increasing coastal hazards in the Yellow Sea region owing to relative sea-level rise. Accordingly, regional studies of such change over the Holocene timescale could be helpful in mitigating these threats. Here, we describe the Holocene record of relative sea-level change in the Gochang-Yeonggwang area of South Korea. We compared this record with that of other sites around the coast of the Yellow Sea, including Bohai Bay (China), the Tando Estuary and Gunsan Bay (South Korea), and sites on the east coast of the South Sea and Toyo-oka Basin, Japan. The findings are based on a multi-proxy study, including lithostratigraphy combined with radiocarbon dating and analyses of grain size distribution, magnetic susceptibility, and geochemistry, which facilitated the generation of 89 paleo-sea-level points reconstructed from 28 borehole cores. The early Holocene transgression was found to start later at Gochang-Yeonggwang than at Gunsan Bay, although the distance between them is only 150 km. This result was inferred from substantial differences in sediment delivery owing to Holocene differences in river basin size, topography, and tectonic context. Before ~7 ka, the slope and highstands from the predicted mean sea-level models at Bohai Bay, Tando Estuary, and Gochang-Yeonggwang were steeper and lower, respectively, from north to south in the Yellow Sea, approaching the slope of the glacio-eustatic sea-level curve. Therefore, the levering effect of transgression in the early Holocene decreased southward in the Yellow Sea. The slight fluctuation in mean sea-level points of the late Holocene resulted from the formation of storm deposit layers in the coastal area, erosion and redeposition in the channel, and geomorphic effects. A partial difference occurred between the relative sea levels at Gochang-Yeonggwang and Toyo-oka. Future relative sea-level research at the southernmost part of the east coast of the Yellow Sea would further improve understanding of the coastal evolution of the region.

1. Introduction

Current threats associated with coastal hazards (coastal erosion, storm surges, and oceanic inundation) will be exacerbated by the projected sea-level rise associated with climate change, with the rate of increase anticipated to accelerate in the 21st century and even beyond (Watson and Lim, 2020). The projected changing rate of mean sea level (MSL) caused by natural factors such as global warming varies from 1.1 mm/y in the north to 4.4 mm/y in the south on the western coast of the Korean Peninsula (Jung, 2014). Early Holocene rapid sea-level rise data are required for predicting future sea-level fluctuations and, considering the importance of agricultural and industrial production on the Yellow Sea coast, research is needed urgently to understand paleo-relative sea-level changes (Yokoyama and Purcell, 2021).

* Corresponding author at: Quaternary Environment Research Center, Korea Institute of Geoscience and Mineral Resources, 124 Gwahak-ro, Yuseong-gu, Daejeon 34132, Republic of Korea.
** Corresponding author at: Center for Earthquake Research and Information, The University of Memphis, 3890 Central Ave, Memphis, TN 38152, USA
E-mail addresses: ydy@kigam.re.kr (D.-Y. Yang), hanmin@kigam.re.kr (M. Han), hhyoon@kigam.re.kr (H.H. Yoon), kjc76@kigam.re.kr (J.C. Kim), echoi2@memphis.edu (E. Choi), shjles2995@naver.com (W.-J. Shin), terraic@chungbuk.ac.kr (J.-Y. Kim), arum@kigam.re.kr (A. Jung), pch304@naver.com (C. Park), cpjun@jnu.ac.kr (C.-P. Jun).

https://doi.org/10.1016/j.palaeo.2023.111779
Received 30 June 2023; Received in revised form 17 August 2023; Accepted 17 August 2023
Available online 24 August 2023

Previous studies have reported rapid sea-level rise in the early Holocene and gradual rise in the mid-Holocene. (Bloom and Park, 1985; Korea Ocean Research and Development Institute, 1994; Chang et al., 1996; Kim et al., 1999; Chang and Choi, 2001; Lee and Chang, 2015). These studies provide missing information from the hydroisostatic adjustment perspective (Song et al., 2018). However, most relevant studies have not provided evidence, such as basal peat, to indicate the beginning of the early Holocene transition. In coastal areas, erosion complicates the intact preservation of sedimentary layers, and basal peat is rarely preserved even on semi-enclosed coasts (Yang et al., 2022). However, relevant reports have been published recently on paleo-sea-level change in Bohai Bay on the northwest coast, the Tando Estuary, and Gunsan Bay on the east coast of the Yellow Sea (Song et al., 2018; Wang et al., 2020; Yang et al., 2022).

Changes in relative sea-level (RSL) are caused by global (glacio-eustatic) sea-level changes and regional land movement (Meijles et al., 2018). Geological observations of postglacial relative land- and sea-level changes in Northwest Europe constrain models of glacial isostatic adjustment (GIA) (Lambeck et al., 1998), which are used to understand the structure of the Earth and the viscosity parameters of the lithosphere and mantle (Vink et al., 2008). Despite the short distance (140 km) between the Tando Estuary and Gunsan Bay, the difference in the early Holocene paleo-mean-sea-level (paleo-MSL) elevation between the sites is substantial (Yang et al., 2022). Yang et al. (2022) suggested that the levering effect caused the significant difference in the elevations between the sites owing to the differences in tectonic characteristics.

Identifying the causes for such early Holocene differences between regions is required, including structural evidence and studying the factors that affect mid- and late Holocene sea-level fluctuations. Accordingly, we obtained relative observed Holocene sea-level data of the study site, which is 50–80 km south of Gunsan Bay, and compared this information with the sea level predicted by the GIA model to confirm the suitability of the data. In addition, we analyzed data from the Geoje and Bibong archeological sites to determine whether the levering effect in the Yellow Sea occurred on the southeast coast of the Korean Peninsula. Our study results provide important data for studying RSL changes in the Yellow Sea, which is the far field of the Western Pacific (Yang et al., 2022). Data are also provided by GIA models on vertical coastal land movement as inputs for future RSL change scenarios (Simpson et al., 2017; Lowe et al., 2018).

2. Site description

Yang et al. (2022) explained the relationship between the tectonic provinces of the North China Craton and those of the Korean Peninsula (Fig. 1a). The Gyeonggi Massif could have a close affinity with the Jiaobei terrane in the North China Craton, and the Okcheon Belt agrees well with the Sulu terrane. However, the Yeongnam Massif is linked more closely to the South China Craton (Liu and Zhou, 2019). The study area and Gunsan Bay corresponding to the Okcheon Belt and the Hwaseong coast (Tando Estuary) belong to the Gyeonggi Massif, and the Bohai region is included in the Eastern Block of the of North China Craton (Fig. 1a).

The Yellow Sea is a semi-enclosed shallow epicontinental sea with an average water depth of approximately 55 m and a maximum depth of 100 m at the southeastern margin (Chough et al., 2000). The seafloor of the Yellow Sea is flat and broad. The tides are semi-diurnal, and the tidal range varies from mesotidal (2–4 m) along the open coast to macrotidal (> 4 m) within the embayments (Oh and Lee, 1998; Cummings et al., 2016). The Gochang-Yeonggwang coast is located on the west coast of Korea in the eastern Yellow Sea. Although most of the west coast of Korea is characterized by rias, our study area has a relatively straight shoreline. Adjacent streams deliver only minor amounts of fine-grained sediment to the coast (Kim et al., 1999). Narrow aeolian dunes are found behind and parallel to the modern beaches. The underlying bedrock comprises Precambrian gneisses and Cretaceous volcanics (Kwon et al., 2015). The Gochang-Yeonggwang coast is macrotidal and semi-diurnal, with a mean tidal range of 4.0 m (Fig. 1b). The spring tidal range is 5.5 m, whereas the neap tidal range is 2.5 m (Korea Hydrographic and Oceanographic Administration, 2013). The Gochang-Yeonggwang coast is exposed to high wave energy, particularly during the winter (Yang and Chun, 2001; Chun and Yang, 2004; Yang et al., 2005; Yoon et al., 2023). The wind regime is marked by pronounced seasonality owing to the monsoonal climate. Weak southerly winds produce mean significant wave heights of 0.4 m during summer, whereas relatively strong northerly winds generate mean significant wave heights of 1.0 m during winter (Korea Meteorological Administration, 2013–2014).

Semidiurnal tides and tidal currents affect the inner shelf near Geoje Island (Fig. 1b and e). The tidal ranges are between 0.3 m (neap tide) and 2.1 m (spring tide) (Korea Hydrographic Office, 1982). Tidal currents are important factors in transporting and dispersing sediments in the nearshore flow west to southwestward during the flood and east to northeastward during ebb with a velocity of 0.4–1.9 m/s at the sea surface (Korea Hydrographic Office, 1982). At the southern tip of Gadeok Island, the path of the tidal currents turns northwest during floods and southeast during ebbs. Superimposed on these tidal currents, the coastal current flows east–northeastward along the coast (Kim et al., 1986). However, the warm Tsushima Current, a branch of the Kuroshio Current, dominates offshore ocean circulation. The current flows northeastward at a typical surface flow speed of 30–90 cm/s and is strongest during the summer (Korea Hydrographic Office, 1982). The strong coastal front between the coastal and saline waters of the Tsushima Current traps fine-grained sediments and prevents their escape to the inner shelf region (Park and Chu, 1991).

River development is insignificant in the Gochang study site (Fig. 1c–d) except for the small Haeri Stream. In the north, facing the research area, two national parks, Byeonsan and Seonunsan, comprise a mountainous area of 300–500 m, with Gomso Bay developed along the coast between them. The Galgok Stream flows through the alluvial layer between the two parks into Gomso Bay, and the Jujin Stream flows into Gomso Bay through Seonunsan National Park. The sediment supplied by these two small streams affects the open coast of the study area after entering Gomso Bay. From Gomso Bay to the reef coast south of the research area, a straight sand coast, called 'Myeongsasipri', is developed in a northeast–southwest direction. In contrast, in the Yeonggwang research area, the Jaryong, Guam, Watan, and Bulgap streams are developed from north to south, all flowing to the coast of the research area. Jaryong Stream flows into the rocky coast of Goripo, and Guam and Watan streams flow into the rocky coast of Beopseongpo. Bulgap Stream, in the south, passes through a relatively large alluvial layer and flows between the sand dunes and mountains to the coast. The lower reaches of these streams are connected to the tidal flats (Figs.1d and S.1–4).

Geoje is the second largest island on the Korean Peninsula, after Jeju Island. Tongyeong, adjacent to the west, and Gadeok Island Busan, located in the northeast, are connected by a bridge. Several ports have been developed because of the mountainous terrain in the northeast and southwest and the curved topography caused by coastal erosion. The reference study area is a small port called Gwanpo, located in the eastern part of the northern tip of Geoje Island (Fig. 1e). The port coast comprises gravelly sand with shells, with villages situated along the coast and salt marshes behind them. Drilling samples were collected from the salt marsh village boundary (GP03) and mountain boundary (GP01).

The downstream flow of the Nakdong River is east and southeast, south again, and into the South Sea. The Holocene sediment layer including Bibong Neolithic remains in the floodplain of the east-flowing section. This site is located approximately 70 km from the mouth of the Nakdong River and is surrounded by low hills 100–150 m above sea level (masl). Before the construction of the Nakdong River Estuary Dam, the plain around Bibong-ri was an inner bay, and the Bibong-ri site was a brackish water station. Diatoms in intertidal and inland environments were identified at altitudes below 1.5 masl. Seawater can be used to

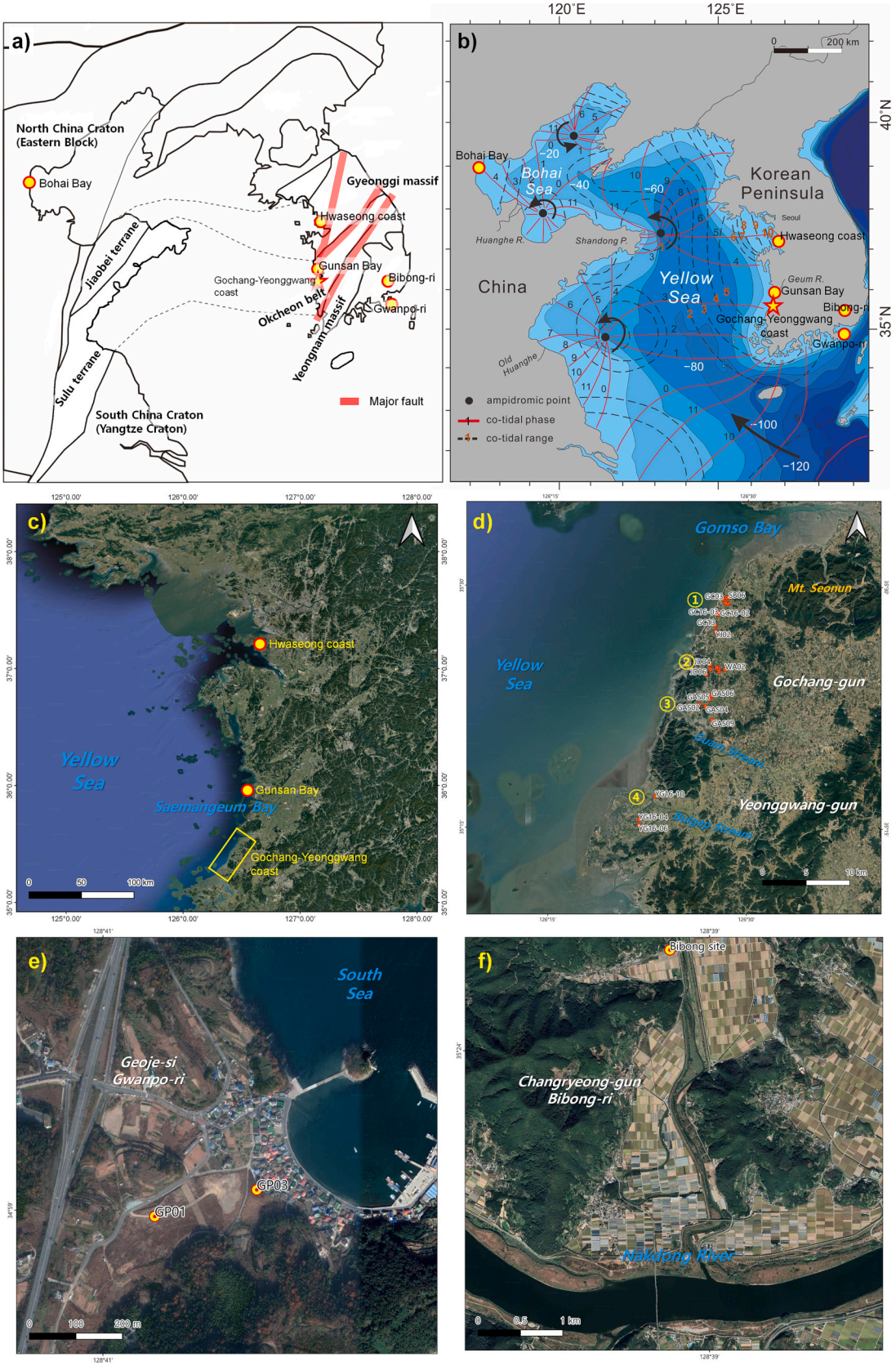

(caption on next page)

Fig. 1. Map of the study area. The yellow circles are the reference sites, and the yellow star is the Gochang-Yeonggwang coastal area study site. a) Geological sketch map showing the tectonic relationships between South Korea and China [modified from Fig. 10 in Liu and Zhou, 2019]. The Gyeonggi massif could have a close affinity to the Jiaobei terrane in the North China Craton, and the Okcheon Belt is consistent with the Sulu terrane. The study area and Gunsan Bay correspond to the Okcheon Belt, with typical fold-thrust belt-related structural architecture (Jang et al., 2015). Conversely, the Bohai region is included in the Eastern Block of the North China Craton. b) Current tidal range information map of the Yellow Sea. Observed tides in the Yellow Sea (M2 tidal only) are modified from Cummings et al. (2015). The tidal current moves northward into the Yellow Sea from the Pacific Ocean. As it shoals across the shelf edge, it shortens in wavelength, is amplified, and subsequently banks up against the right-hand (eastern) side of the Yellow Sea basin because of the Coriolis effect. This generates meso- to macro-tidal conditions along the west Korean coast. The reflected tidal wave moves from the Yellow Sea along the Chinese coast. The interference of incoming and reflected waves produces four amphidromous systems in the Yellow and Bohai seas. Because of tidal friction and energy dissipation, the reflected wave is weaker than the incoming wave, displacing the amphidromic points toward the Chinese coast. c) Satellite image map of the study site (yellow square box) with the Hwaseong coast and Gunsan Bay reference sites. d) Satellite image map of the study site including four subdivisions of ① Saban-ri and Gwangseung-ri subarea; open coast, ② Jindeok-ri subarea; boundary of open coast and rocky coast, ③ Guam Stream basin subarea with the barrier of rocky coast, ④ Bulgap Stream basin subarea; open coast with a north rocky coast. e) Satellite image map of Gwanpo Port of the east face in the northernmost of Geoje Island. The borehole locations are paleo-tidal zone. GP01 and GP03 correspond to the slope and village ends of the salt marsh. f) Satellite image map of Bibong, the archeological site, approximately 70 km from the mouth of the Nakdong River. The plains around the Bibong site were an inner bay, and the site was a brackish water area (Hwang et al., 2013). (For interpretation of the references to colour in this figure legend, the reader is referred to the web version of this article.)

remove tannins from acorns, and acorn silos have been excavated from several coastal layers. Moreover, shell mounds were found in five separate layers, with some containing exposed traces, through which, together with diatomic analysis, human activity was confirmed to have occurred near the shoreline or salt marshes (Hwang et al., 2013).

3. Methods

We secured 26 borehole cores in the salt marsh and intertidal zones of the surveyed area (Fig. 1c–d) and two borehole cores at the reference site, Geoje Gwanpo Port (Fig. 1c, d, e). X-ray fluorescence (XRF) analysis was performed on the 28 borehole core samples at 2 cm intervals. Subsequently, organic materials such as wood chips or charcoal were collected for radiocarbon dating, and subsampling was performed at 2 cm intervals for the next analysis. After drying the collected samples, their magnetic susceptibilities and grain size distributions were analyzed. After comprehensively interpreting the analyzed data and confirming the sedimentary facies, the paleo-MSL was calculated from the depth and formation age of each sedimentary layer. A predicted GIA model was generated and compared with the observed data. Dating, grain size distribution, and magnetic susceptibility analyses are routine tasks performed in the laboratory at the Korea Institute of Geoscience and Mineral Resources (KIGAM). Therefore, except for chemical analysis, the method employed in Yang et al. (2022) was applied in this study.

3.1. Radiocarbon age dating

Radiocarbon (^{14}C) age dating confirmed the ages of the sedimentary environmental changes at the study site. First, 91 radiocarbon samples were collected from the 28 drilling cores (Tables 1 and 4). The radiocarbon dating objects were terrestrial plant fragments included horizontally in the deposited layer. The collected samples were subjected to chemical pretreatments and oxidation-reduction processes to produce the graphite targets. The ^{14}C ages were measured employing the accelerator mass spectrometer (AMS) owned by the KIGAM for the finished graphite targets. The ^{14}C ages were calculated and converted to calendar dates using the applications IntCal13 (Reimer et al., 2013) and OxCal v4.3.2 (Ramsey, 2017) (Table 1). Optically stimulated luminescence (OSL) dating was employed only for identifying pre-Holocene sedimentary layers and is excluded from the general discussion.

3.2. Grain size distribution and magnetic susceptibility analyses

To confirm the change in and distribution of the grain size characteristics of sediments, grain size analysis was performed on the collected sediment. Chemical pretreatment was performed to accurately analyze the grain size distribution of the samples. The grain sizes of the pretreated samples were measured using a laser particle analyzer (Mastersizer 3000; Malvern Instruments, Ltd., Worcestershire, UK) owned by KIGAM. For the measured data, the particle size distribution characteristics were analyzed using the logarithmic graphical measures method of Folk and Ward (1957) employing the software GRADISTAT Version 8.0 (Blott and Pye, 2001).

Magnetic susceptibilities were measured using a portable magnetic susceptibility meter (ZH-instruments SM30, Czech Republic) with sensitivity of 10^{-7} SI. Each data point was checked twice or thrice to ensure signal reproducibility. The soil samples were placed in a sealed polyethylene cube and dried for three days. The magnetic susceptibilities of the plastic cubes were measured in a laboratory using a Bartington MS2 susceptibility bridge (Bartington Instruments Ltd., United Kingdom).

3.3. Chemical analysis

Radu and Diamond (2009) analyzed the soil pollution concentration around a mine using a portable XRF radioisotope and miniature tube-powered analyzer (NITON Instruments, Thermo Fisher Scientific, MA, USA). A comparison of the performances of the portable XRF instrument and a laboratory-based reference atomic absorption spectrometer (AAS) showed excellent correlation. Hunt and Speakman (2015) suggested that an XRF spectrometer could not accurately quantify Na, P, V, Cr, Co, Ni, and the L lines of Ba in an archeological ceramic or sediment matrix. These authors compared the results of quantitative analyses using wavelength dispersive XRF (WD-XRF), instrumental neutron activation analysis (INAA), and/or inductively coupled plasma-mass-spectrometry (ICP-MS). However, the results of the remaining major and trace elements, such as Sr, Zr, and Rb, agree with other quantitative analysis results. Employing an Olympus Delta-professional p-XRF instrument (Olympus IMS, MA, USA) produced chemical analysis values for the borehole core samples from the study site without XRF analysis preparation, such as subsampling, drying, and grinding. The core samples were analyzed by scanning three times for 30 s at 2 cm intervals for main and trace element analyses. Major elements were indicated as oxide wt %, and minor and trace elements reported in ppm (Hunt and Speakman, 2015).

3.4. GIA model

A paleo-MSL prediction model for the Gochang-Yonggwang region was created by applying the method employed in Yang et al. (2022), as follows. The RSL changes at selected locations in the study area during the Holocene were calculated using SELEN4 (Spada and Melini, 2019), an open-source code that solves the sea-level equation (Farrell and Clark, 1976; Clark et al., 1978; Peltier and Tushingham, 1989). This equation governs changes in global sea-level through the melting of ice sheets and the time-dependent response of the solid Earth to ice and water mass redistribution, termed glacial isostatic adjustment (GIA).

Table 1
^{14}C age dating results in the coastal area of Gochang-Yeonggwang.

Borehole Name	Sample Lab. No.	Material	Depth/ Elevation (m)	^{14}C Age (BP)	δ^{13}C
GC03	KGM-ITg140819	Wood	2.96/0.54	2080 ± 80	−25.40 ± 0.60
GC03	KGM-ITg140834	Wood	6.37/−2.87	7870 ± 140	−31.50 ± 1.50
GC03	KGM-ITg140832	Wood	6.17/−2.67	7700 ± 90	−31.40 ± 1.40
GC03	KGM-ITg140830	Wood	5.16/−1.65	7630 ± 50	−24.80 ± 0.90
GC03	KGM-ITg140828	Wood	4.35/−0.85	7510 ± 70	−25.90 ± 0.60
GC13	KGM-ITg140908	Wood	3.29/0.11	410 ± 100	−11.20 ± 2.30
GC16–02	KGM-ITg170111	Shell*	3.49/0.11	2440 ± 30	0.20 ± 0.70
GC16–02	KGM-ITg170112	Shell*	3.70/−0.10	2470 ± 30	3.10 ± 2.60
GC16–03	KGM-ITg170113	Wood	1.68/1.42	160 ± 30	−26.20 ± 2.20
GC16–03	KGM-ITg170114	Wood	3.38/−0.18	1110 ± 30	−25.70 ± 1.00
SB01	KGM-ITg150446	Wood	3.53/0.73	7350 ± 80	−27.90 ± 0.60
SB02	KGM-ITg150535	Wood	2.46/1.04	1510 ± 100	−32.40 ± 0.80
SB02	KGM-ITg150536	Wood	2.65/0.85	1620 ± 80	−32.30 ± 1.00
SB02	KGM-ITg150554	Wood	3.18/0.32	2150 ± 150	−24.80 ± 1.10
SB03	KGM-ITg150477	Wood	1.75/2.25	230 ± 230	−28.90 ± 1.40
SB03	KGM-ITg150478	Wood	1.85/2.15	160 ± 150	−32.10 ± 0.80
SB03	KGM-ITg150479	Wood	1.95/2.05	140 ± 120	−27.90 ± 1.00
SB03	KGM-ITg150449	Wood	4.02/−0.02	7670 ± 90	−30.90 ± 1.00
SB03	KGM-ITg150450	Wood	4.79/−0.79	7550 ± 110	−31.80 ± 0.90
SB05	KGM-ITg151706	Wood	3.50/−0.10	7590 ± 90	0.40 ± 0.30
SB06	KGM-ITg151691	Wood	5.72/−2.42	7830 ± 110	−27.50 ± 0.20
YJ02	KGM-ITg150486	Wood	2.73/0.47	1730 ± 100	−28.50 ± 0.90
YJ02	KGM-ITg150542	Wood	3.94/−0.44	7350 ± 80	−30.60 ± 0.60
JD01	KGM-ITg150467	Wood	5.89/−3.09	7530 ± 80	−31.60 ± 0.50
JD02	KGM-ITg150436	Wood	7.61/−4.11	7930 ± 90	−31.30 ± 0.60
JD02	KGM-ITg150472	Wood	7.47/−3.97	8150 ± 160	−31.10 ± 0.70
JD02	KGM-ITg150468	Wood	3.83/−0.33	5440 ± 130	−27.10 ± 0.50
JD02	KGM-ITg150470	Wood	6.52/−3.02	7830 ± 130	−29.80 ± 2.00
JD02	KGM-ITg150435	Wood	7.01/−3.51	7920 ± 130	−31.50 ± 0.50
JD02	KGM-ITg150471	Wood	7.26/−3.76	8020 ± 140	−29.80 ± 0.50
JD03	KGM-ITg150445	Wood	4.65/−0.65	7450 ± 120	−35.70 ± 0.80
JD03	KGM-ITg150437	Wood	2.52/1.48	430 ± 90	−32.40 ± 0.80
JD03	KGM-ITg150438	Wood	2.90/1.10	710 ± 40	−32.90 ± 0.40
JD03	KGM-ITg150439	Wood	3.14/0.86	3100 ± 110	−30.40 ± 0.40
JD04	KGM-ITg160607	Wood	4.88/−2.78	7800 ± 130	−30.70 ± 1.20
JD05	KGM-ITg160609	Wood	3.46/−0.76	6670 ± 130	−32.80 ± 0.40
JD06	KGM-ITg160610	Wood	2.80/0.90	2180 ± 140	−31.10 ± 0.30
JD06	KGM-ITg160611	Wood	3.55/0.15	2250 ± 100	−28.40 ± 0.40
JD06	KGM-ITg160612	Wood	5.80/−2.10	7800 ± 130	−36.30 ± 0.60
JD06	KGM-ITg160613	Wood	6.74/−3.04	8080 ± 100	−30.70 ± 0.40
GAS02	KGM-ITg162672	Wood	6.08/−3.58	7580 ± 90	−28.50 ± 0.30
GAS02	KGM-ITg160622	Wood	6.47/−3.97	7890 ± 100	−15.20 ± 1.30
GAS02	KGM-ITg160623	Wood	12.02/ −9.52	8440 ± 100	−27.80 ± 1.40
GAS04	KGM-ITg151707	Wood	2.40/−0.70	2270 ± 110	−4.06 ± 0.40
GAS04	KGM-ITg151708	Shell*	2.65/−0.95	2530 ± 180	−1.30 ± 0.70
GAS04	KGM-ITg151699	Wood	6.63/−4.93	8020 ± 160	−30.60 ± 1.20
GAS04	KGM-ITg160615	Wood	11.03/ −9.33	8230 ± 160	−35.20 ± 1.00
GAS05	KGM-ITg160616	Wood	2.60/0.50	160 ± 150	−34.90 ± 1.00
GAS05	KGM-ITg160617	Wood	8.96/−6.86	8370 ± 150	−25.90 ± 0.50
GAS05	KGM-ITg151702	Wood	3.50/1.00	3090 ± 130	−27.20 ± 0.60
GAS09	KGM-ITg160629	Wood	1.38/1.62	5080 ± 210	−32.20 ± 0.70
GAS09	KGM-ITg162673	Wood	2.51/0.49	4700 ± 130	−30.20 ± 0.40
GAS09	KGM-ITg160630	Wood	2.92/0.08	7440 ± 120	−28.60 ± 0.50
GAS09	KGM-ITg162674	Wood	3.25/−0.25	7360 ± 80	−27.50 ± 0.10
YG16–10	KGM-ITg170207	Wood	4.58/−0.38	6440 ± 300	−26.50 ± 0.50
YG16–10	KGM-ITg170208	Wood	4.80/−0.60	6610 ± 390	−26.40 ± 0.40
YG16–10	KGM-ITg170209	Wood	5.47/−1.27	6770 ± 390	−30.60 ± 0.70

The SELEN4 code requires a history of ice melting associated with an assumed radial viscosity profile. Two of three combinations distributed using SELEN4 were used in this study. These are the ice-melting models ICE-5G, based on the viscosity profile VM2r (Peltier, 2004), and ICE-6G, based on VM5a (Peltier et al., 2015). SELEN4 uses the present-day global topography model ETOPO1 (Amante and Eakins, 2009; Eakins and Sharman, 2012) to calculate the lateral movement of shorelines. All the calculations were conducted on a Tegmark grid (Tegmark, 1996) with a resolution of 44, corresponding to a uniform resolution of 46.31 km. All fields were expanded by spherical harmonics up to 476°, which is the maximum allowed on the chosen grid. The complete set of input parameters and a list of locations where the RSL changes were calculated are provided as supplementary information.

3.5. Sea-level indicator proxies

Sea-level indicator proxies for the Gochang-Yonggwang region were created by applying the method in Yang et al. (2022). The relationships between the paleo-sea level of the basal peat and salt marsh were applied to the peat proxy (Wang et al., 2013; Wang et al., 2020), and those of the intertidal zone were also applied to each corresponding proxy (shown in Table 2). Recently, major maritime countries, including the USA, Australia, and the UK have adopted the lowest astronomical tide (LAT) and highest astronomical tide (HAT) as tidal datums. The LAT (HAT) values are, on average, 33.6 (46.2) cm lower (higher) than the

Table 2
Reference local tide gauges of the study site and the differences between local tide (National Geographic Institute, 1983; 1996) and astronomical tide in Incheon (Byun et al., 2019).

Water level (m)	Beopseongpo*	Tongyeong*	Water level (m)	Incheon**
Highest high water (HHW)	3.25	3.59	Highest astronomical tide (HAT)	5.10
Mean spring high water (MSHW)	2.67	0.94	Highest high water (HHW)	4.68
Mean high water (MHW)	2	0.59	(HAT-HHT)	0.42
Mean neap high water (MNHW)	1.34	0.19		
Mean sea level (MSL)	0.02	−0.23	Mean sea level (MSL)	0.00
Mean neap low water (MNLW)	1.3	−0.65		
Mean low water (MLW)	−1.97	−1.02	(LAT-LLW)	−0.65
Mean spring low water (MSLW)	−2.63	−1.39	Lowest low water (LLW)	−4.68
Lowest low water (LLW)	−3.22	−1.64	Lowest astronomical tide (LAT)	−5.33

approximate lowest low water (ALLW) and approximate highest high water (AHHW) values along the west and south coasts of Korea (Byun et al., 2019). The ALLW and AHHW have been used as tidal level data for paleo-MSL studies in the Yellow Sea. We used the current tide gauge data of Beopseongpo (National Geographic Institute, 1983) and Tongyeong (National Geographic Institute, 1996) to convert the dated layer into sea-level index points (SLIPs) for comparison with the results of recent studies on the paleo-sea-level in the Yellow Sea (Table 3). Beopseongpo is located within the study area and Tongyeong on the right side of Geoje, approximately 40 km from the Nakdong River Delta. Based on the indicative paleo-MSL shown in Table 4, the free R package ggplot2 was employed to plot the RSL curve in the study area. The red line and shaded area represent the loess smooth curve (span 0.3) and 95% confidence interval (Fig. 7). The sedimentation rate was extracted based on the slope of the red line.

4. Results

The research area was divided into four subareas from north to south, namely 1) Saban-ri and Gwangseung-ri subarea of open coast; 2) Jindeok-ri subarea, the boundary of open coast and rocky coast; 3) Guam Stream subarea with barrier of rocky coast; 4) Bulgap Stream subarea of open coast, of which the research results are described (Fig. 1b). Because subareas 1 and 4 are open coast, waves had a significant impact on the deposition mechanism during 6–1 ka (Yoon et al., 2023). Subareas 2 and 3, which are semi-open shores, appear to have been affected less by wave erosion. Among the intertidal zones, erosion from wave effects was lower in small valleys than in flatlands. However, because of erosion, a large number of sediments deposited in the 8–7 ka and 2–1 ka range dominate. After cutting the drilling core at the drilling site, the sedimentary facies and colors on the core were observed and, after subsampling in the laboratory, grain size, magnetic susceptibility, and geochemical analyses were performed.

In the study area, the sediment colour in the drilling core provided important information. The Holocene marine sediments are bluish gray, whereas the salt marsh sediments are dark gray to black. However, the Pleistocene marine sediments are gray to yellowish gray. Shell fragments and traces of organic matter are present in the intertidal zone. Sand is often present in intertidal zones and appears as sand-balls, sand-films, and sandy silt layers with small shell fragments. Salt marsh sediments were distinguished easily because they contain abundant organic matter and were formed in pre-Holocene sediment beds or bedrock, Pleistocene sediments, or marine sediments during the rapid sea-level rise in the early Holocene. In the late Holocene, salt marshes formed on the intertidal sedimentary layer, which occasionally remained as swamps until recently.

The intertidal zone sediments could have been supplied from slope sediments through the water system or moved from the surrounding sea or subtidal zone through currents, waves, or storm surges. Because currents and waves are regimes that move and deposit sediments, sedimentation characteristics vary depending on the transporting energy. A bivariate plot of mean grain size against sorting for the sediment core of the study site is shown in Fig. 3. The relationships of the simplified sedimentary facies are shown in Fig. 3a, where most points of swamp sediments are in low-energy and good sorting regions, but those in tidal flats are scattered by influx of dune sand or slope sediments. This tendency is most prominent in the straight sea areas of Saban-ri and Gwangseong-ri subareas and weakest in the Guam Stream subarea with a rocky barrier (Fig. 3b). Because magnetic fine iron oxides exist in silt and clay materials on slope sediments, high magnetic susceptibility indicates an increase in the inflow of slope sediments. However, the magnetic susceptibility decreases if fine particles are swept away by waves or currents after inflow, with only coarse materials remaining.

Drilling core samples from the study area were analyzed for major and trace elements. The values of major elements such as SiO_2, Al_2O_3, Fe_2O_3, K_2O, and MnO showed different patterns depending on the sedimentary layer. If Fe_2O_3 and MnO increased simultaneously, Fe-Mn clusters were probably formed by the groundwater flow. Increased SiO_2 and K_2O contents imply increased slope sediment inflow (Yang et al., 2016). Sulfur can exist as sulfate or sulfide, even in swamps on land; however, sulfur derived from seawater is the main source in coastal areas. Therefore, the change in sulfur content is an indicator of the influence of the sea. Chlorine content was used as an auxiliary indicator. Zirconium deposited on the coastline often moves to the supratidal zone because of storm surges or waves, and changes in the Zr content of beaches and sediments accumulated by such phenomena

Table 3
Proxy types and the estimation processes of paleo-mean sea level (paleo-MSL) at the indicative sedimentary boundaries.

Borehole Name	Sedimentary environment	Related proxy	Relationship to sea level	Altitude (m)	Error range (m)	Calibrated age (ka)	Paleo-MSL (m)
GAS02	basal peat	peat	MSHW-MHW[1]	−9.52	±0.34	8.44 ± 10	−11.86 ± 0.34[a]
GAS04	basal peat	peat	MSHW-MHW[1]	−10.2	±0.34	8.41*	−12.54 ± 0.34[b]
JD04	salt marsh	peat	MSHW-MHW[1]	−3.9	±0.34	8.16*	−6.24 ± 0.34[c]
YG16–10	lower boundary of intertidal flat	tidal flat	MHW-MLW[2]	−1.8	±1.98	6.8*	0.18 ± 1.98 [d]
JD01	upper boundary of intertidal flat	tidal flat	MHW-MLW[2]	−2.69	±1.98	7.53 ± 85	−4.67 ± 1.98[e]
JD03	upper boundary of intertidal flat	tidal flat	MHW-MLW[2]	1.48	±1.98	0.43 ± 95	−0.5 ± 1.98[f]

[a] ; −9.52-(MHW+(MSHW-MHW)/2) ± (MSHW-MHW)/2, [b]; −10.2-(MHW+(MSHW-MHW)/2) ± (MSHW-MHW)/2, [c];-3.9-(MHW+(MSHW-MHW)/2) ± (MSHW-MHW)/2, [d]; −1.8 + (MHW-MLW)/2 ± (MHW-MLW)/2, [e]; −2.69-(MHW-MLW)/2 ± (MHW-MLW)/2, [f]; 1.48-(MHW-MLW)/2 ± (MHW-MLW)/2, [1]; Wang et al., 2013, [2]; Chang et al., 1996; Wang et al., 2013, *; ages by extrapolation of two nearby points.

Table 4
Reconstruction of indicative paleo-MSL based on the sedimentary sea level in the study site.

Borehole name	Sedimentary environment	Elevation (m)	Age (ka, cal yr BP)			Paleo-MSL (m)		
JD01	Upper intertidal flat	−2.69	7.53	±	0.09	−4.67	±	2
JD02	Salt marsh (peat)	−4.11	7.93	±	0.09	−6.45	±	0
JD02	Salt marsh (peat)	−3.97	8.15	±	0.16	−6.31	±	0
JD02	Intertidal flat	−3.76	8.02	±	0.15	−3.76	±	2
JD02	Intertidal flat	−3.51	7.92	±	0.13	−3.51	±	2
JD02	Intertidal flat	−3.02	7.83	±	0.13	−3.02	±	2
JD02	Intertidal flat	−2.87	7.53	±	0.08	−2.87	±	2
JD02	Intertidal flat	−0.33	5.44	±	0.14	−0.33	±	2
JD03	Salt marsh (peat)	−0.65	7.45	±	0.13	−2.99	±	0
JD03	Salt marsh (peat)	−0.48	7.4	±	0.09	−2.48	±	0
JD03	Intertidal flat	−0.21	7.35	±	0.08	−0.21	±	2
JD03	Intertidal flat	0	7.3	±	0.13	0	±	2
JD03	Intertidal flat	0.19	7.1	±	0.14	0.19	±	2
JD03	Intertidal flat	0.48	6.1	±	0.1	0.48	±	2
JD03	Intertidal flat	0.86	3.1	±	0.11	0.86	±	2
JD03	Upper intertidal flat	1.48	0.43	±	0.1	−0.5	±	2
JD03	Salt marsh (peat)	1.1	0.71	±	0.05	−1.24	±	0
JD04	Lower intertidal flat	−2.51	3.77	±	0.12	−0.53	±	2
JD04	Salt marsh (peat)	−3.37	8	±	0.16	−5.71	±	0
JD04	Intertidal flat	−2.78	7.8	±	0.13	−2.78	±	2
JD05	Intertidal flat	−0.76	6.67	±	0.13	−0.76	±	2
JD06	Coast	−3.04	8.08	±	0.1	−5.38	±	0
JD06	Salt marsh (peat)	−2.1	7.8	±	0.13	−4.44	±	0
JD06	Intertidal flat	0.15	2.25	±	0.1	0.15	±	2
JD06	Intertidal flat	0.9	2.18	±	0.14	0.9	±	2
GAS01	Intertidal flat	−1.4	2.56	±	0.18	−1.4	±	2
GAS02	Intertidal flat	−0.53	0.49	±	0.1	−0.53	±	2
GAS02	Intertidal flat	−3.58	7.58	±	0.09	−3.58	±	2
GAS02	Intertidal flat	−3.97	7.89	±	0.1	−3.97	±	2
GAS02	Basal peat (peat)	−9.52	8.44	±	0.1	−11.86	±	0
GAS04	Intertidal flat	−0.7	2.23	±	0.11	−0.7	±	2
GAS04	Intertidal flat	−0.95	2.53	±	0.18	−0.95	±	2
GAS04	Intertidal flat	−4.93	8.02	±	0.17	−4.93	±	2
GAS04	Basal peat (peat)	−9.33	8.23	±	0.16	−11.67	±	0
GAS05	Intertidal flat	0.5	0.16	±	0.15	0.5	±	2
GAS05	Lower intertidal flat	−6.86	8.37	±	0.15	−4.88	±	2
GAS06	Beach-supra tidal	1	3.09	±	0.13	−1.34	±	0
GAS09	Beach-supra tidal	1.62	5.08	±	0.21	−0.72	±	0
GAS09	Intertidal flat	0.49	4.7	±	0.13	0.49	±	0
GAS09	Intertidal flat	0.08	7.44	±	0.12	0.08	±	0
GAS09	Intertidal flat	−0.25	7.36	±	0.08	−0.25	±	2
GC13	Intertidal flat	0.11	0.41	±	0.1	0.11	±	2
GC16–03	Salt marsh (peat)	1.42	0.16	±	0.03	−0.92	±	0
GC16–03	Intertidal flat	−0.18	1.11	±	0.03	−0.18	±	2
GC03	Intertidal flat	0.54	2.07	±	0.08	0.54	±	2
GC03	Intertidal flat	−2.87	7.87	±	0.15	−2.87	±	2
GC03	Intertidal flat	−2.67	7.7	±	0.1	−2.67	±	2
GC03	Intertidal flat	−1.65	7.63	±	0.06	−1.65	±	2
GC03	Intertidal flat	−0.72	7.35	±	0.08	−0.72	±	2
SB01	Intertidal flat	−0.73	7.35	±	0.1	−0.73	±	2
SB01	Lower intertidal flat	−3.92	7.41	±	0.1	−1.94	±	2
SB01	Intertidal flat	1.04	1.51	±	0.1	1.04	±	2
SB02	Intertidal flat	0.85	1.62	±	0.09	0.85	±	2
SB02	Intertidal flat	0.32	2.15	±	0.15	0.32	±	2
SB03	Salt marsh (peat)	2.25	0.23	±	0.23	−0.09	±	0
SB03	Salt marsh (peat)	2.15	0.16	±	0.16	−0.19	±	0
SB03	Salt marsh (peat)	2.05	0.14	±	0.12	−0.29	±	0
SB03	Upper intertidal flat	1.23	7.35	±	0.14	−0.75	±	2
SB03	Intertidal flat	−0.02	7.67	±	0.1	−0.02	±	2
SB03	Lower intertidal flat	−0.79	7.55	±	0.12	1.19	±	2
SB04	Salt marsh (peat)	2.32	2	±	0	−0.02	±	0
SB05	Intertidal flat	0.1	7.47	±	0.13	0.1	±	2
SB06	Lower intertidal flat	−2.02	7.83	±	0.11	−0.04	±	2
WA02	Salt marsh (peat)	−0.09	7.44	±	0.12	−2.43	±	0
WA02	Upper Intertidal flat	1.37	1.52	±	0.11	−0.61	±	2
YG16–05	Intertidal flat	0.2	3.9	±	0.34	0.2	±	2
YG16–06	Intertidal flat	−2.27	5	±	0.34	−0.29	±	2
YG16–06	Lower intertidal flat	−1.73	2.48	±	0.34	0.25	±	2
YG16–10	Beach-supra tidal	2.08	0.76	±	0.3	−0.26	±	0
YG16–10	Intertidal flat	0.93	6.12	±	0.3	0.93	±	2
YG16–10	Intertidal flat	0.12	6.37	±	0.3	0.12	±	2
YG16–10	Intertidal flat	0.02	6.31	±	0.3	0.02	±	2
YG16–10	Intertidal flat	−0.38	6.44	±	0.3	−0.38	±	2

(*continued on next page*)

Table 4 (*continued*)

Borehole name	Sedimentary environment	Elevation (m)	Age (ka, cal yr BP)			Paleo-MSL (m)		
YG16–10	Intertidal flat	−0.6	6.61	±	0.4	−0.6	±	2
YG16–10	Lower intertidal flat	−1.27	6.77	±	0.4	0.71	±	2
YG16–10	Lower intertidal flat	−1.86	6.8	±		0.18	±	2
YJ02	Lower intertidal flat	0.9	1.67	±	0.11	0.9	±	2
YJ02	Intertidal flat	0.47	1.73	±	0.11	0.47	±	2
YJ02	Intertidal flat	−0.44	7.35	±	0.09	−0.44	±	2
Gwanpo-ri of Geoje Island in east southern Korean Peninsula								
GP01	Salt marsh (peat)	1.65	1.24	±	0.07	0.9	±	0
GP01	Salt marsh (peat)	1.55	1.54	±	0.1	0.8	±	0
GP01	Salt marsh (peat)	1.44	1.64	±	0.08	0.69	±	0
GP01	Salt marsh (peat)	1.33	1.96	±	0.01	0.58	±	0
GP01	Salt marsh (peat)	1.18	2.25	±	0.1	0.43	±	0
GP03	Salt marsh (peat)	0.6	0.34	±	0.13	−0.15	±	0
GP03	Salt marsh (peat)	0.12	1.35	±	0.05	−0.63	±	0
GP03	Intertidal flat	−0.81	2.6	±	0.14	−0.81	±	1
GP03	Intertidal flat	0.06	1.45	±	0.09	0.06	±	1
GP03	Lower intertidal flat	−1.45	3.9	±	0.18	−0.65	±	1
Bibong archeological site in the tributary of the Nakdong River in east southern Korean Peninsula								
BB	Salt marsh (peat)	−2.05	7.53	±	0.06	−2.8	±	0
BB	Salt marsh (peat)	0.48	5.83	±	0.15	−0.27	±	0
BB	Salt marsh (peat)	0.8	6.01	±	0.04	0.05	±	0
BB	Salt marsh (peat)	0.59	5.48	±	0.05	−0.16	±	0
BB	Salt marsh (peat)	0.65	5.21	±	0.04	−0.1	±	0

could be considered as estimates of such events (Yang et al., 2016). Strontium is related highly to shells and shows changes similar to those of CaO; however, only strontium was high because CaO is eluted easily during weathering. Phosphorus pentoxide (P_2O_5) is generally related to the organic matter content, and Ba represents marine productivity (Costa et al., 2009).

4.1. Saban-ri and Gwangseung-ri subarea

This subarea corresponds to the straight coast north of the study area (Figs. 1c–d and S.1). Sand dunes are developed well along the coast, and a windbreak forest of pine trees was established on these dunes in the 1960s and 1970s (Park et al., 2007), stabilizing the sand inside the dunes. The area behind the dunes was mainly used as a rice field and appeared to have been a back marsh or intertidal zone (GC03, SB01 and 05 cores), depending on the degree of dune development during the Holocene. Mountainous hinterland areas are mainly low hills at altitudes of 20–80 masl, with small valleys formed between the hilly areas. The slope of the small valley from borehole SB01 (2.76 masl) to SB04 (3.85 masl) was 0.27% gentler. Before reclamation, swamps were formed near boreholes SB02, 03, and 06, and sedimentary layers, presumably salt marshes in the past, were confirmed in these boreholes. The direct impact of dunes was minimal approximately 500 m from the shore (borehole GC03). The ~7 ka intertidal flat underlying the ~2 ka sandy silt layer, approximately 3 m thick, contains an intercalated layer of storm sand approximately 1 m thick (Fig. S.5, borehole core GC03). The 7–8 ka beach sand layer underlying the intertidal flat overlies the bedrock (GC03) or Pleistocene intertidal sediments (SB01 and 03, Fig. S.5, SB01 and 03). Considering that the upper part of the Pleistocene intertidal zone was exposed to a shallow depth of −0.7 to −0.5 masl, boreholes SB02 and 04 (Fig. S.5 SB02 and 04), would have served as breakwaters to protect sediments from erosion, and formed swamps. In this area, salt marshes were formed at 2.3–2.5 masl after ~2 ka (SB03 and 04).

Borehole SB01 (Fig. S.5 SB01) corresponds to the intertidal zone, and the grain size of the sedimentary layer is exceptionally small, except for the lowest sand layer. Magnetic susceptibility shows a slight splashing section (including pyrite) but is generally constant and decreases in the sand layer. In boreholes SB02 and 04 sediments (Fig. S.5, SB02 and 04), the grain size splashes on a section, apparently related to the inflow of small amounts of coarse particles (Fig. 3b). As the top section of SB04 core sediments show a coarse grain size and high magnetic susceptibility, it was considered to have experienced substantial inflow from the slope sediments and organic matter. However, SB03 core sediments show a relatively thick sand layer, significantly increasing the grain size; however, the magnetic susceptibility in the section decreased. A prominent part of the magnetic susceptibility appeared to be related to pyrite (Fig. 4a). In borehole SB06, the upper part showed a very fine grain size, whereas the sandy bottom part showed a very large grain size deviation. Magnetic susceptibility appeared inversely proportional to the grain size change pattern, although it was usually within a small range (Fig. S.5, SB06). The origin of this sediment was likely sand from the subtidal zone carried by typhoons. In borehole GC03, magnetic susceptibility increases upward in the upper sand layer of the intertidal zone at 7 ka and in the upper sand layer of the intertidal zone with a high sand content at 2 ka (Fig. S.5, GC03). It was inferred that a significant amount of slope sediment had been introduced into this layer.

Regarding drilling core sediments in the study area, the blue-gray and shell-fragmented layers were all considered intertidal with a high sulfur content and partially intertidal with high chlorine, strontium, and zirconium contents. Additionally, sections presumed to be brackish or saline marshes were identified using this concept. In the uppermost sedimentary layer of SB03 (Fig. 4a), the grain size is small, but the phosphorus and zirconium contents are high; therefore, it was presumed a salt marsh affected by the sea. The upper part of SB04 shows a large grain size, high magnetic susceptibility, and high phosphorus content, indicating substantial inflow of sediment and organic matter from the slope. The area was estimated to be a brackish swamp because of the increase in the sulfur and Sr contents in the lower part (Fig. S.5, SB04). As regards the 4.79–7 m SB03 depth section, a sand layer occurs with an extremely change in grain size and slightly high magnetic susceptibility. The Zr content of this layer is highly variable and increases rapidly. The phosphorus content increases and subsequently decreases, whereas the sulfur content increases. These features are also evident in storm deposits (Chagué-Goff, 2010). In contrast, in the 2 m depth section of SB02, SiO_2, Al_2O_3, K_2O, and Fe_2O_3 show peaks with increased magnetic susceptibility, but that of S decreases (Fig. S.5, SB02).

4.2. Jindeok-ri subarea

The small Jaryong Stream flows through Goripo, the boundary between the straight beach and the rocky coast (Figs.1b and S.2). This basin is short and small, but narrow valleys have developed, such as Jindeok-ri on the right and Seoknam-ri on the left bank, and the

Holocene salt marsh and tidal sediments are relatively well preserved. Sampling was performed by drilling at the following points in both valleys, namely boreholes in JD01, 02, 03 and JD04, 05, 06 (Fig. S.5, JD01 to 06). The slopes between the drilling boreholes of JD01 (2.5 masl), JD02 (2.9 masl) and JD03 (4.2 masl) in the Jindeok-ri Valley are low at 0.15% and 0.25%, respectively, and tend to increase slightly inside the valley. In the next valley, the section from the tidal flat (borehole JD04, 1.97 masl) to the valley (JD05. 2.4 masl) has a slightly larger slope of 0.43%. In these terrains, sea-level fluctuations are well documented, and sediments in the form of salt marshes are commonly observed. Borehole JD03 was a swamp until recently. The Holocene intertidal flat where borehole JD04 is located overlies a Pleistocene tidal flat that has been eroded. Holocene tidal flat sediments (~5.47 m depth at 8 ka) contain slope sediments and organic matter introduced into the valley entrance intertidal zone. In borehole JD01, the Holocene intertidal deposit, approximately 9 m thick (Fig. S.5 JD01), overlies the Pleistocene tidal flat (approximately 3 m thick) with a boundary with bedrock at 14.4 m depth. A fluvial sand layer, approximately 1.5 m thick, is intercalated between the tidal flat layers. In tidal sediments, sediments rich in organic matter and sand are easily distinguishable from subsections (starting at 7 ka from the tidal zone), as are the 3–6 m deep sections. Holocene sediments are thinner in the valley interior (JD02, 5.7 m thick; JD03, 3.74 m thick), but the inflow patterns of organic matter and slope sediments are similar (Fig. S.5, JD02 and 03). In particular, salt marshes existed at the boundary between Pleistocene and Holocene intertidal sediments during 8 ka and 7.4 ka (JD02, 7.4–7.7 m deep; JD03, 5.4–5.8 m deep).

Cores JD04 and 05 show similar sedimentary facies in ascending order, with an intertidal zone at 8–7 ka, another tidal flat at ~3 ka, and a sandy silt layer at ~0.8 ka (Fig. S.5, JD04 and 05). The sedimentary layers after 3 ka show substantial variations in grain size and remarkable magnetic susceptibility. In borehole JD06 from the upper valley, the upper part of the drilling core shows a sandy silt layer at 2 and 7 ka (Fig. S.5, JD06). The magnetic susceptibility shows a remarkable change in the layer at 7 ka. Apparently, the sediments on the slopes inflowed or remained during the process of erosion by ocean currents and waves (Fig. 3). The salt marsh layer comprises silt or clay underlying the sandy silt layer of 7 ka and, although the magnetic susceptibility is high, it is generally stable.

In the JD01 sediments, a sand layer with a large variation in grain size is located in the altitude range − 2.6 m to 0 m, the SiO_2 and K_2O values are increased, with sulfur and chlorine decreasing simultaneously. Therefore, this layer was estimated to be the event layer caused by storms, with an upper intertidal layer at ~7 ka underlying the layer (Fig. S.5, JD01). A similar pattern was observed in borehole JD04, except for a high chlorine content. A layer at ~3 ka overlies the upper intertidal flat of ~7 ka. Pleistocene intertidal deposits underlie lower intertidal flats. Intercalated salt marshes increased the sulfur, strontium, and organic matter contents at their boundaries. This phenomenon also appears in borehole JD03, where a salt marsh layer rich in organic matter is distributed at the boundary between the intertidal and Pleistocene intertidal zones (Fig. S.5, JD03). In this layer, sulfur exhibits large fluctuations. In contrast, the SiO_2 and K_2O contents are decreased. In the JD06 drilling core, sulfur increases in the organic-rich sand layer underlying the fluvial sand layer, and the zirconium and strontium contents are high (Fig. S.5, JD06). Owing to sea-level rise, the river sand layer appears to have accumulated as a beach when it met seawater. The upper layer appears to be a clayey or silty salt marsh layer rich in organic matter. The sulfur and zirconium contents increase significantly, and the strontium content is also high.

4.3. Guam Stream basin subarea

Guam Stream in the north flows to the southwest, and Watan Stream in the south flows to the northwest, joining at Beopseongpo, passes between the rocky shores of mountains at 200–400 m, and flows into the sea (Figs. 1d and S.3). The downstream basins of these rivers are relatively large areas where tidal flats are reclaimed, with numerous low hills and small valleys distributed between them. Samples were obtained by drilling downstream of the Guam Stream. Samples GAS02 and GAS04 were collected from a relatively wide intertidal zone, and samples GAS05, 06 and 09 from the valley (Fig. S.5, GAS02, 04, 05, 06 and 09). Therefore, the tidal flats and valley entrances are dominated by silty sediments and the valleys by sandy sediments. Borehole GAS02 is located at the mouth of a small valley, and GAS04 at the mouth of a large valley and stream. Consequently, with rapid transgression, the sediments of GAS02 were deposited on Pleistocene tidal flats, and those of GAS04 on alluvial sand deposits when the deposition started at 8.3 ka to 8.5 ka. This effect led to the mean grain size distribution in the former gradually increasing upward, and its variation increasing from 7.8 ka to 0.6 ka. However, in GAS04, the grain size distribution decreases upward, and its fluctuation is smaller after 5 ka (Fig. 4c and d).

Magnetic susceptibility has several peaks in GAS02 but, generally, has small values and is constant in GAS04 (Fig. 4c and d). During the early transgression, a silty salt marsh formed in the former because of minimal channel influence, and a sandy silt marsh formed on the fluvial sand deposits in the latter because of the channel influence. Borehole GAS09 was drilled inside the southern valley of the Guam Stream (Figs.1d and S.3). An intertidal flat 3 m thick overlying fluvial deposit with rapid transgression (Fig. S.5 GAS09). In addition, salt marshes and coastal sand layers deposited on top. A slight change in the grain size was observed but no significant peak. The peaks increased along with increasing magnetic susceptibility; however, with apparently insignificant relationship with grain size distribution.

The upper sediments were deposited after 2 ka (GAS01) or 4 ka (GAS09), and the lower sediments mostly formed in the range 7–8 ka, which has a boundary with the Pleistocene tidal flat (GAS02 and 05) or fluvial deposits (GAS04, 06, and 09). Pleistocene tidal flats remained at the mouth of the valley, and sandy layers were deposited adjacent to the Guam Stream or at the top of the valley (Fig. S.5 GAS series). Except for the sedimentary layer formed at 4 ka in borehole GAS09 in the upper valley, the sedimentary layers formed between 6 and 3 ka were hardly identified. The lower part of the Guam Stream comprises a wide tidal flat with an open rocky barrier. Sedimentation proceeded rapidly during the transgression but, after 6 ka, as sea-level rise slowed and the tide-dominant environment switched to a wave-dominant environment, erosive activity in the wave impingement zone apparently increased (Yoon et al., 2023).

Sediments in the Guam River basin generally belong to low-energy well-sorted regions (Fig. 3). The borehole core sediments of GAS02 and GAS04 show contrasting mean grain size distribution. GAS02 increased upward and showed a large fluctuation at the top, while GAS04 gradually decreased, showed fluctuations in the middle, and then decreased further (Fig. 4c and d). The magnetic susceptibility of GAS02 tended to decrease gradually as it increased, and for GAS04, several large peaks appeared at the top. However, the correlation with grain size was small. In contrast, for GAS09, the grain size changed depending on the sand content, and the magnetic susceptibility gradually increased (Fig.S.5 GAS09). This phenomenon is similar to that observed for GAS06 (Fig.S.5 GAS06). Therefore, the influence of the slope sediment on the sediment layer in these areas gradually increased.

The borehole GAS02 section at the small valley entrance contains Holocene intertidal sediments over Pleistocene intertidal sediments. The sulfur, chlorine, and zirconium contents began to increase in the salt marshes formed at the boundary (Fig. 4c). The contents of these elements reached their maximum after passing 7.58 ka. This phenomenon occurred similarly to Jindeok-ri subarea at 2–3 ka. GAS04 was located at the mouth of a large valley close to a river that gave rise to Holocene deposits overlying fluvial sand deposits. The grain size decreased upward, but the sulfur and chlorine contents increased (Fig. 4d). Sulfur reached its maximum value at 2–3 ka, whereas chlorine decreased. A peak of CaO in the −0.95–1.3 m altitude range is an effect of the high

inclusion of oyster shells. In contrast, in the −0.5–0.4 m section of the GAS09 (Fig.S.5 GAS09), the sulfur content increased significantly during ~7 ka, and the chlorine content increased slightly. The upper part showed a large variation in the magnetic susceptibility, and MnO showed a similar change. Although Fe_2O_3 did not differ much, it did change. In addition, P_2O_5, sulfur, and strontium exhibited variations. Therefore, it was estimated that this section experienced high groundwater flow after the formation of a salt marsh with a large amount of organic matter.

4.4. Bulgap Stream basin subarea

The southernmost part of the study area is where the rocky coast ends, and the Bulgap Stream subarea, which has a relatively wide basin, flows into the Yellow Sea (Figs. 1d and S.4). Currently, the strong sea breezes facilitate the generation of wind power. Dunes are developed widely on the downstream west bank, and dunes approximately 5 km long and at maximum 1.6 km wide, with a maximum height of 30 m are currently developed 1–3 km from the coast. Dunes are currently used in residential areas and fields. Drilling was done between the dunes and the river (YG16–06). Borehole YG16–10 is located in Yaksu-ri at the end of the northern rock beach and is not influenced significantly by sand dunes. This borehole is a back-sand dune close to the stream, and it was inferred that intertidal silt deposits were intercalated several times when the influence of the dune weakened (Fig. S.5, YG16–06). The intercalated layer contains several shell fragments from the intertidal flats. Sedimentary layers that formed at 2.72 and 5.24 ka were identified at −1.73 and − 2.27 masl, respectively, suggesting strong erosion activity between them (Fig. S.5, YG16–06). In borehole YG16–10 (Fig. 4e), intertidal sediments are predominant, apart from the sand at the top. Layer boundaries between sand and silt in the core sediments were interpreted as supratidal environments because the silt–sand layer contain organic matter. At an elevation of 2.08 m, coastal sediments formed at 0.76 ka, and the lower 0.93 m to 1.27 m section formed at around 6 ka are preserved well; therefore, most sediments formed middle period were found to have eroded after 6 ka. A layer with angled gravel and abundant upper organic matter was identified between altitudes −0.8 and − 0.98 m, which was presumably introduced from events such as storms. Bedrock was identified at the bottom and is viewed as the boundary of the sedimentary layers of the intertidal zone (Fig. 2).

In the borehole sediments cores of YG16–05 and − 06, intertidal and dune sediments appear alternately (Figs. 3b and S.5, YG16–05 and − 06). Because the borehole is located at the rear of the sand dune in contact with the Bulgap Stream, it appears that the influence of the dune and seawater were alternately affected, which appears to be related to seasonal changes in the intertidal zone (Yang et al., 2005). The mean grain size is large in the dune sediments but small in the intertidal sediments. Sediments with large variations in grain size are distributed in the lower intertidal zone. Intertidal sediments that appear as underlying coarse sediments remained after the existing sand layers had been eroded by storms. Magnetic susceptibility showed only one peak at the boundary between the intertidal zone and the dune layer, with no significant change. The boreholes of drilling point YG16–10 were at the end of a rocky beach to the north and were unaffected by dunes (Fig. 3b). The mean grain size increased in the upper sandy regions, was extremely

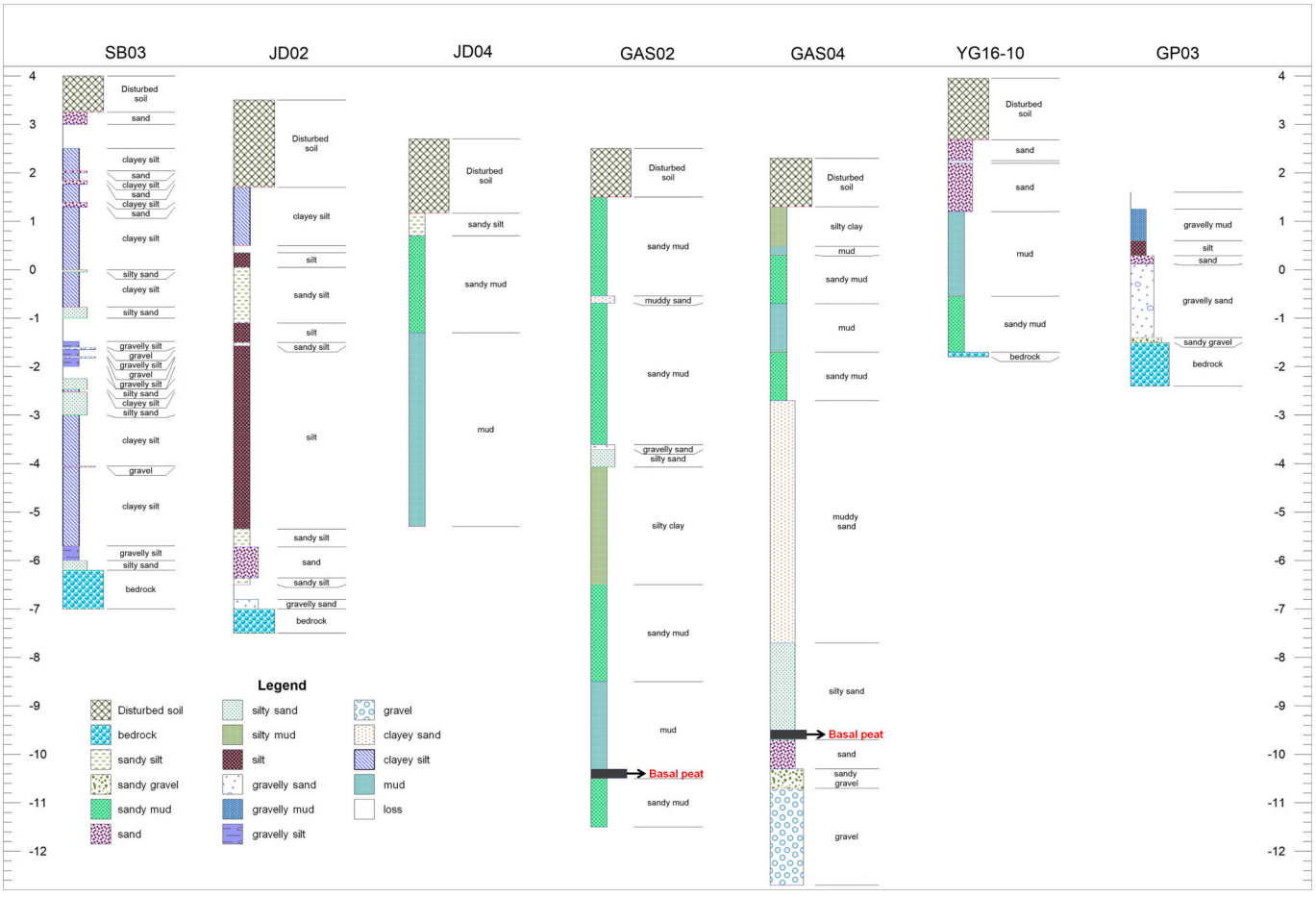

Fig. 2. Sedimentary layers of the representative boreholes on the Gochang-Yeonggwang coast and the Gwanpo Port reference site. Basal peat layers are intercalated between Pleistocene and Holocene tidal flats (GAS02) or between Pleistocene streams sand layers and Holocene tidal flats (GAS04). SB; Saban-ri, JD; Jindeok-ri, GAS; Guam Stream, YG; Yeonggwang (Bulgap Stream), GP; Gwanpo Port.

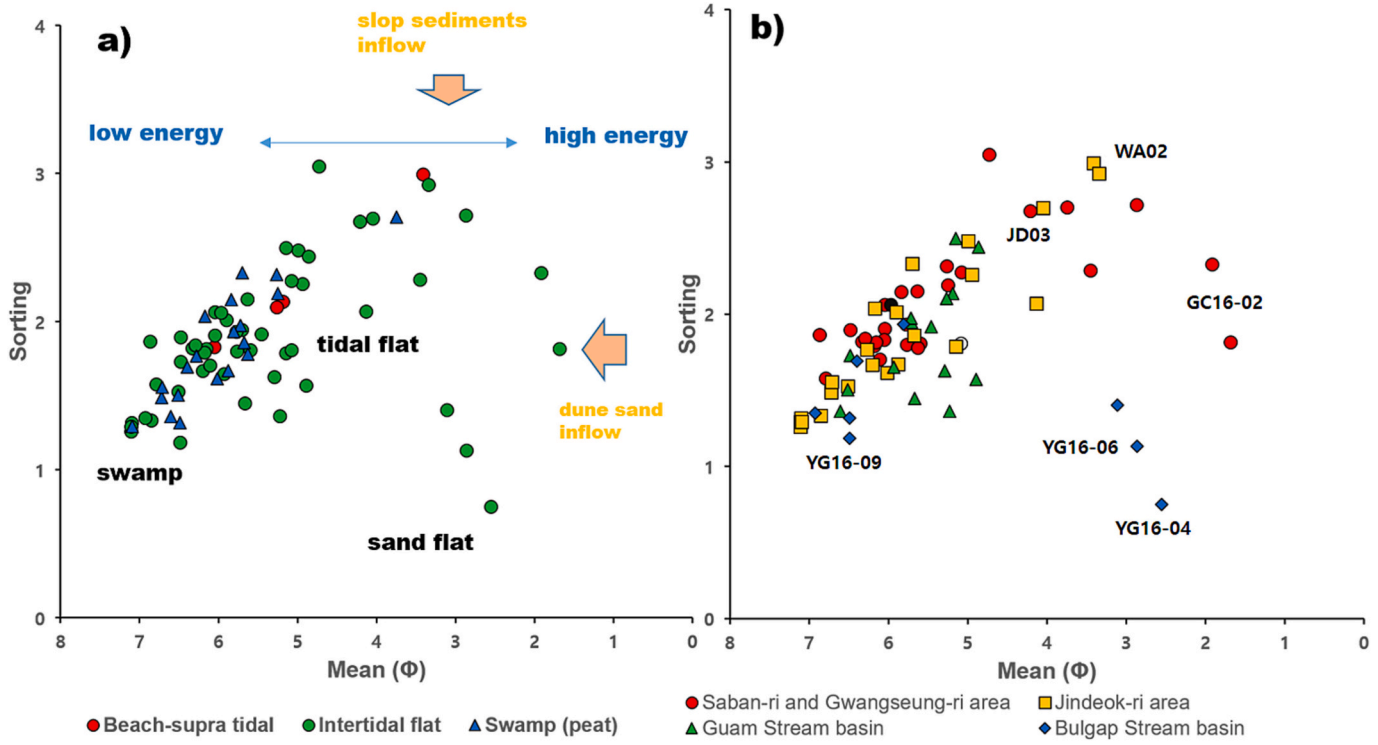

Fig. 3. Mean grain size (φ)-sorting diagram of borehole sediments in the study site. a) Grain size distribution in the four subdivided areas. Most sediments show a pattern of poor sorting as the grain size increases; however, the three points of the Bulgap Stream (lower right; blue diamond) are coarse owing to the influence of the sand dunes. Some Saban-ri (red circle) sediments are dispersed under the influence of sand dunes. b) Grain size distribution classified by sedimentary characteristics. Swamp samples (blue triangles) show a stable deposition environment. SB; Saban-ri, JD; Jindeok-ri, GAS; Guam Stream, YG; Yeonggwang (Bulgap Sream), GP; Gwanpo Port. (For interpretation of the references to colour in this figure legend, the reader is referred to the web version of this article.)

low in the intertidal zone, slightly increasing downward. The lowest part has a large grain size, but magnetic susceptibility is low in all sections except the upper part.

The chemical compositions of YG16–05 and − 06 cores differ significantly between the intertidal and dune-affected layers (Fig. S.5, YG16–05 and − 06). The strontium content is generally high but variable, particularly in the layer affected by dunes. The sulfur and zirconium contents are high in the intertidal layer, which agrees well with the aforementioned mean grain-size distribution values. In borehole YG16–10, Zr shows substantial fluctuation and subsequently decreases at the boundary between the sandy mud and the muddy intertidal flat. Strontium also shows a decrease, and sulfur an increase with a large peak out of the boundary (Fig. 4e).

4.5. Sediment characteristics of boreholes GP01 and 03 of Gwanpo Port, as a reference site

The section sediments of borehole GP01 between 1.61 and 2.25 m in elevation were evaluated as salt marsh sediments because they contain abundant organic matter with a fine grain size and low magnetic susceptibility, as well as a high sulfur content (Fig. S.5, GP01). The upper layer is rich in organic matter but appears to be a freshwater marsh sedimentary layer as the sulfur content decreases suddenly. As borehole GP03 is located in a boundary area with the intertidal zone, thin salt marsh sediment is located at 0.6–0.12 masl, and the lower part is connected to the intertidal zone (Fig. 4f). The grain size fluctuates significantly, and the magnetic susceptibility decreases upward. The CaO content also fluctuates significantly owing to the influence of shells. The sulfur content is distributed over the entire range, but decreases upward.

The Gwanpo coast, located east of the northernmost part of Geoje Island, comprises gravelly sand with shells and is affected mainly by waves. Behind a coastal village, a salt marsh is spread close to the mountainous valley. Borehole core samples were collected and analyzed from borehole GP03, adjacent to the village, and borehole GP01, adjacent to the mountain valley along the salt marsh margins. The upper portion of GP03 core sediment is salt marsh sediment formed at 0.06 to −0.81 m elevation during 0.14 to 1.35 ka, and the lower portion is shelly gravelly sand coastal sediment. In contrast, the upper part of the latter (GP01) was a brackish swamp, and the lower part a salt marsh at 0.43–0.9 m elevation during 1.24–2.25 ka. Considering that some salt marsh sediments (approximately 40–50 cm in thickness) in the upper part of GP03 were disturbed and eroded by human intervention, it could be inferred that the salt marsh sediments of GP03 slightly overlap those of GP01.

4.6. Estimating the paleo-MSL based on the sedimentary sea-level proxy

Typhoon Rusa, which caused the most substantial damage in Korea in 2002, passed through the Baeksu coast, the southernmost part of the study area, and created a hummock mound and a deep channel in the mudflat. Storm beds in Baeksu coast have been reported by Yang et al. (2005), confirming that numerous topographical changes in the intertidal zone and sedimentary layers resulting from such storm events could have been deposited frequently in the coastal land areas. In the northern part of the study area, the sand layer deriving from such events was estimated to have been deposited in the altitude range − 0.79 m to −3 m at ~7 ka in borehole SB03 core sediments. The sand layer intercalating the mud layers was distinguished easily; however, it was difficult to distinguish when a mud layer was inserted between them. Therefore, layers with a substantial age difference in the intertidal flat were excluded from the paleo-MSL estimation.

Coastal sedimentary facies can be used as paleo-sea-level proxies based on changes in the Holocene sedimentary environment (Chang et al., 1996; Fan et al., 2013; Wang et al., 2013; Song et al., 2018). The

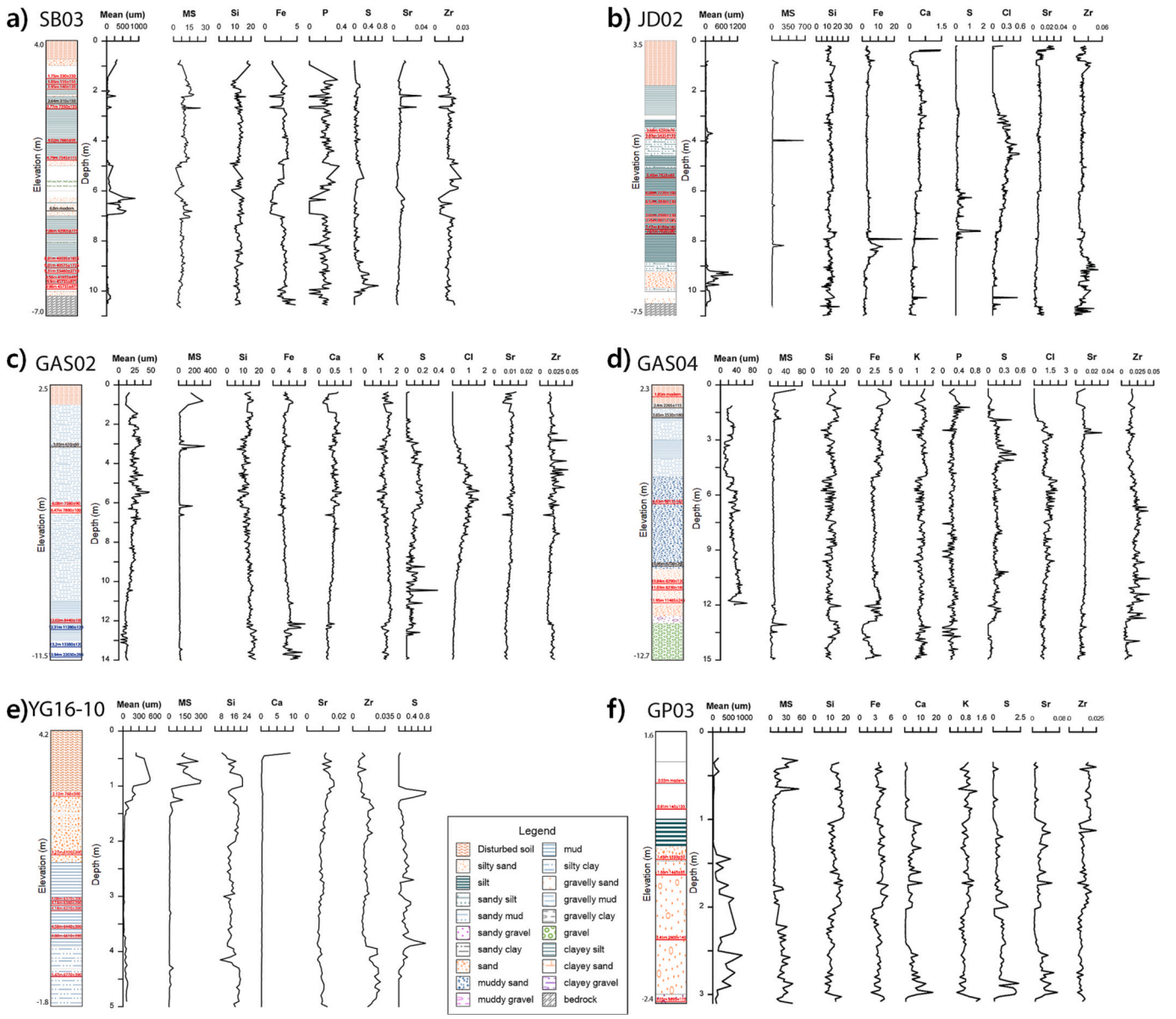

Fig. 4. Physicochemical characteristics of the representative borehole sediments as sedimentary layers, mean grain size (μm), MS (magnetic susceptibility; 10^{-5} SI unit), and several major and minor elements. Altitude is indicated in the column and depth within the graph. The physicochemical characteristics were used as auxiliary indicators to determine S, Cl, Sr, Zr, and Cl; marine effect, Ca; shell and magnetic susceptibility, and other major elements; the inflow effect of slope sediment. SB; Saban-ri, JD; Jindeok-ri, GAS; Guam Stream, YG; Yeonggwang (Bulgap Sream), GP; Gwanpo Port.

characteristics of the sediments, including grain size, magnetic susceptibility, organic matter, and chemical content were used to identify the sedimentary sea-level proxies of the basal peat layer, intertidal flats, and salt marsh. Indicators of the RSL, which have a definite relationship with the past MSL (as described in Section 3.5, Table 3) are usually called SLIPs. Indicative paleo-MSLs were reconstructed based on these proxies (Table 3). Basal peat beds, salt marshes, and intertidal deposits were used to establish Holocene relative MSLs. In addition, although not the main subject of this study, we considered the RSL data of Geoje and Bibong in the eastern part of the South Sea of the Korean Peninsula, reconstructed from tidal flats and salt marsh sediments (Table 4), for comparison with the paleo-sea-level behavior in the study area during the Holocene. Table 3 shows suggested proxy types and estimation processes for paleo-MSL at the indicated sedimentary boundaries. The basal peat bed in GAS02 and 04 cores were confirmed at −9.52 and −10.2 m elevation at 8.44 and 8.41 ka, respectively (Table 3).

The paleo-MSLs estimated from the peat layer as a salt marsh were −11.86 and − 12.54 m, respectively, using the relationship of mean spring high water (MSHW) to mean high water (MHW), shown in Table 3 (Chang et al., 1996; Wang et al., 2013). However, in the latter case, the elevation extended to the boundary of the Pleistocene bed, and the age was converted by extrapolating two nearby points. This process was also applied to the salt marsh bed in JD04 (Table 3), which was confirmed at −3.9 m in elevation at 8.16 ka, with the paleo-MSL estimated at −6.24 m. In contrast, the estimated ranges of paleo-MSLs from the upper (JD01 and 03) and lower (YG16–10) boundaries of intertidal flats are shown in Table 4. At an elevation of −2.69 m of the JD01 borehole, a boundary was observed between the upper part of the intertidal sediment, with abundant organic and sandy silt, and the lower part of the homogeneous silty intertidal flat. Further, the lower boundary of the intertidal flat at an elevation of −1.73 m of borehole YG16–10 was distinguished from bedrock. Table 3 shows the estimated paleo-MSLs (Chang et al., 1996; Wang et al., 2013; Song et al., 2018). Table 3 also shows the estimation processes of the indicative paleo-MSL reconstruction for six of the 27

borehole cores, and Table 4 shows those of the remaining reconstructed 21 cores, The above process was similarly applied to reconstruct the paleo-MSL of each sampling point at the Gwanpo Port of Geoje Island and the Bibong archeological sites (Table 4). The reference local tide gauges of Tongyoung near the two sites were used instead of those of Beopsong-po (Table 2). Hwang et al. (2013) reported the location and elevation range of each sediment layer where samples were collected at the Bibong site. In the current study, the average elevations of each layer were obtained, and the elevation deviations were included in the error ranges to estimate the paleo-MSL at the Bibong site (Table 4).

4.7. Model predictions for RSL changes at the study site

The calculated RSL changes in the study area after 11 ky BP are shown in Fig. 5, along with the results for Nanyang Bay. Results based on the ice-melting hysteresis model, ICE-6G, indicated a change of approximately −20 m at approximately 11 ky BP. The RSL increased quasi-linearly to approximately +4 m × 6.5 ky BP before decreasing to the current sea level (0 m) at a much slower rate. The ICE-5G-based RSL variants followed the same pattern but were consistently lower than the ICE-6G-based results. The ICE-6G- and ICE-5G-based models of Gochang were used at lower elevations than those of Namyang Bay.

5. Discussion

Records of RSL are scarce, particularly for the Yellow Sea of Northeast Asia. According to the limited research data available, the beginning of the early Holocene transgression was indicated employing basal peat on the east coast of the Yellow Sea. Early Holocene transgression data based on basal peat excavated from the Tando Estuary can be used to compare the beginning of transgression between the study site and other areas of Bohai and Gunsan bays (Yang et al., 2022). The significant difference in elevations observed between Tando Estuary and Gunsan Bay was caused by the levering effect of the different tectonic characteristics. We compared the observed and predicted paleo-MSL from the study site and two other sites to discuss the differences between them and estimate the causes.

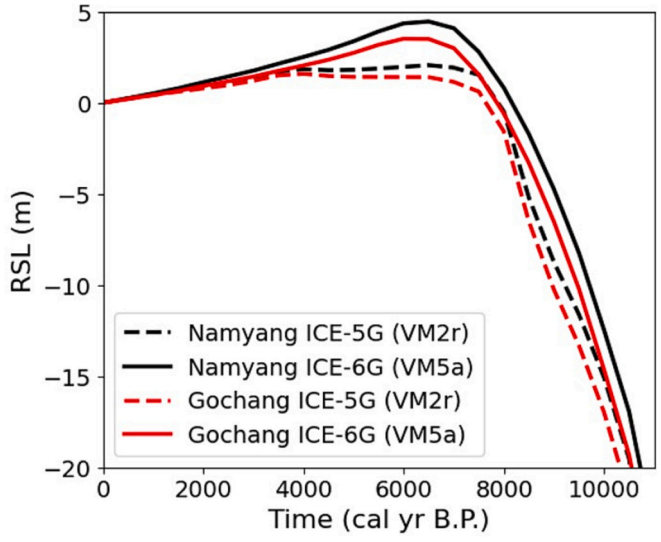

Fig. 5. Calculated relative sea level (RSL) changes in the study area after 11 ky BP shown along with the Namyang Bay results. The RSL and age data for the study site and two RSL changes predicted by SELEN4 (Spada and Melini, 2019) based on the ICE-6G (solid line) and ICE-5G (dashed line) glacier melt history models.

5.1. Comparison of the study site and other sites in the sedimentation environment

Preferably, in paleo-MSL estimations, salt marshes and intertidal flats without significant terrain changes caused by typhoons should be employed. Intercalated sand layers are commonly distributed in the coastal lands of the open sea of the study area (borehole SB03) owing to storm surges. The basal peat formation environment was estimated to be formed between MSHW and MHW (Chang et al., 1996; Wang et al., 2013). Recently, using the basal peat layer of the Tando Estuary, the paleo-MSL was estimated at −15.4 ± 0.52 m at approximately 10.3 ka (Yang et al., 2022). During the early Holocene transgression, silty and sandy silt basal peat formed on the Pleistocene tidal flat (borehole GAS02) and the fluvial sand deposits (borehole GAS04) at the study site (Fig. 2). Their paleo-MSLs were estimated at −11.86 m at 8.44 ka in borehole GAS02 and − 12.54 m at 8.41 ka in borehole GAS04 (Table 4). The onset of transgression in the study site was later and shallower than it was in the other sites of Bohai Bay (−17.2 m at 9.7 ka), Tando Estuary (−15.4 m at 10.3 ka), and Gunsan (−27.9 m at 9.8 ka). Yang et al. (2022) explained why the Tando Estuary formed earlier, despite being relatively higher than Bohai Bay, as follows. Bohai Bay has a small tidal difference of 3–4 m, whereas that of the Tando Estuary is large (8–9 m). Bohai Bay is an open coast, but the site is semi-enclosed; therefore, pre-Holocene erosion and early Holocene depositional patterns differed between the regions. The sediments in Bohai Bay were deposited mainly along shorelines (Wang et al., 2020), but through pre-Holocene and/or early-formed channels in the Tando Estuary. The Gochang-Yeonggwang coast study area shows characteristics of both Bohai Bay and the Tando Estuary. The straight open north coast has characteristics of the former, whereas Beopseong Port, where the Guam and Watan streams join and flow in the Yellow Sea, has characteristics of the latter, as it has a rocky coastal barrier with a relatively large tidal difference of 6–7 m (Fig. 1b and d).

In Gunsan Bay, Holocene sedimentary facies are divided into three sedimentary units in ascending order, namely basement to tidal flat with silt in the early Holocene, marine transgression with sandy silt in the middle Holocene, and tidal flat with silt in the late Holocene (Bak, 2015). The stratigraphy of the Namyang Bay intertidal zone near the Tando Estuary comprises a Pleistocene tidal flat, early Holocene mud, and mid- to late Holocene intertidal flat showing upward coarsening. Previous study shows unconformities between the early and mid-Holocene and between the Holocene and late Pleistocene (Lim et al., 2003). Unconformities within mid-Holocene deposits generally occur along the eastern coast of the Yellow Sea. Sedimentary layers eroded at 6–4 ka in Tando Estuary (Yang et al., 2022), 5–3 ka in Gunsan Bay (Song et al., 2018), 7–2 ka in the open sea, and 6–3 ka in the valley of the study area. Yoon et al. (2023) contended that the RSL rise rate affects the transition from a tidal-dominated (10–6 ka) to a wave-dominated environment (6–1 ka), as well as sedimentation rates in shelf settings. The enhanced wave energy after the rapid uplift of the RSL from 10 to 6 ka is a major factor in the erosion and redeposition of the existing sedimentary layer at 6–1 ka (Yoon et al., 2023). The degree of erosion varied depending on the topography of the survey area.

5.2. Comparison of the early Holocene sedimentation environment and the sea-level rise rate of Gunsan Bay and the study site

The early Holocene sea-level rise rate in the study area was 20.1 mm/a, much higher than 4.5 mm/a in the Tando Estuary, 6.4 mm/a in Bohai Bay, and 14 mm/a in Gunsan Bay. However, the rates in the study area appear temporarily high, as shown by their short range (8.41–8.16 ka). This value is similar to those of Tando Estuary and Bohai Bay to 5.8 mm/a, from 8.16 to 7.10 ka of the highstand in the middle Holocene. As mentioned above, sedimentation rates vary considerably because the sedimentation environments of each site differ. Despite the proximity of Gunsan Bay to the survey area, a difference was observed in the

sedimentation rates. To understand the cause, a comparison of the environmental factors, such as topography and water systems is required.

Gunsan Bay meets the southern end of the Chugaeryeong fault zone, which is almost north–south (Yang et al., 2022). The Gunsan Bay area would have deepened because of the influence of the Chugaryeong fault zone and the Geum River, the third largest in Korea. This river is a channel for the transport of large amounts of water and sediment but, during the last glacial maximum (LGM), the sediment supply decreased and the channel deepened (Oh et al., 2010). However, at the study site, Pleistocene sediments remain in shallow areas because there are no large rivers and areas where fault zones intersect. The early Holocene transgression at the study site started later and at a shallower layer than that at Gunsan Bay, for which the lowest indicative paleo-MSL is −27.9 m at 9.8 ka, inferred from the peat layer in the lagoon (Song et al., 2018). As the transgression at the study site started at −11.86 m elevation at 8.44 ka, a substantial difference occurred between the two sites in the start time and elevation of the transgression. However, if sedimentation was achieved at a sedimentation rate of 14 mm/a in Gunsan Bay during 1.36 ka of a time difference (9.8–8.44 ka) between the start of transgression in the two regions, it increased by approximately 19.04 m and the expected altitude at 8.44 ka in Gunsan Bay would be approximately −9 m (−27.9 m + 19.04 m). As it was found approximately 3 m higher than approximately −12 m at 8.44 ka in the study area, this was assumed a reasonable value considering the size of the river basins in the two areas. In contrast, although Gunsan Bay is extremely deep, the transgression of Gunsan Bay at 9.8 ka was rather late compared with that of the Tando Estuary at 10.3 ka. Therefore, probably, a process must have occurred where sediment was deposited along the channel, eroded, and redeposited at a depth exceeding −27.9 m and more rapidly than 9.8 ka.

Accordingly, as discussed above, although the two regions are 150 km apart, the distribution patterns of paleo-MSL were inferred to differ because the substantial differences in sediment inflow indicated the size of the river basin and the pre-Holocene topography and tectonic characteristics. Therefore, it is reasonable to compare the observed and predicted values by applying different prediction models.

5.3. Observed and predicted paleo-MSL in the study and other sites

Testing and refining of GIA models can be achieved by comparing their local predictions of RSL history with geological inferences based on appropriate sea-level indicators (Roy and Peltier, 2018). However, such refinement could not sufficiently explain the difference in early Holocene sea-level fluctuations in the Tando Estuary and the Bohai and Gunsan bays employing only sedimentary mechanisms (Yang et al., 2022). Therefore, the GIA model for the Tando Estuary was developed using SELEN4 (Spada and Melini, 2019). The observed and predicted values matched well during the early Holocene; however, the values in the Tando Estuary differed from those in Gunsan Bay. The Gunsan model was a result set based on the tectonic structural characteristics of the South China Sea or Malay Peninsula (Bradley et al., 2016). The paleo-MSL of the Tando Estuary during the early Holocene was similar to the predicted value of the Bohai model. The tectonic characteristics of the Gyeonggi Massif and Okcheon Belt differed substantially (Koh et al., 2015; Liu and Zhou, 2019). To some extent, the Okcheon Metamorphic Belt could be a tectonic characteristic of the South China Craton because the lithological and geochemical data from the Neoproterozoic metavolcanic rocks in the belt show similarities with the Nanhua Rift in South China, revealing a North Asian connection associated with the disruption of the Rodinia Supercontinent (Kim et al., 2006). The Gochang-Yeonggwang area is within 150 km of Gunsan Bay, but the observed

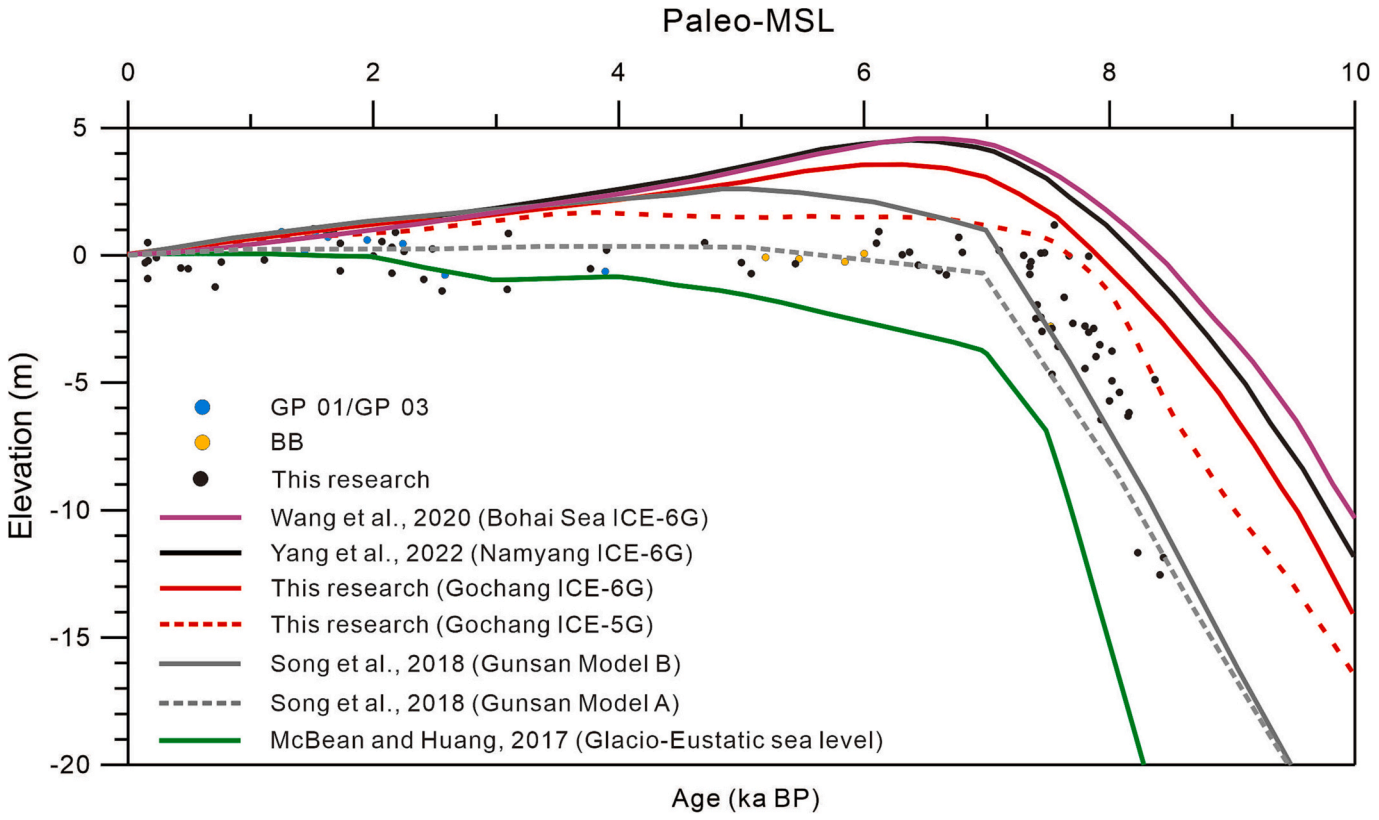

Fig. 6. Comparison of the predicted models produced for the Yellow Sea coast. The slope of the early Holocene model is steep from Bohai Bay, the most inland, to Gunsan Bay, close to the Pacific Ocean. The green line represents the glacio-eustatic sea level, and Model A of Gunsan Bay is closest to this line. The Gunsan Bay models are based on the structural characteristics of Southeastern China (Bradley et al., 2016; Song et al., 2018). (For interpretation of the references to colour in this figure legend, the reader is referred to the web version of this article.)

paleo-MSL of the study area differs slightly from that of Gunsan Bay. Accordingly, we developed the study area GIA model employing SELEN4, similar to that used for the Tando Estuary (red and broken lines in Fig. 6). The Gunsan Bay GIA model (Song et al., 2018) was reconstructed using the parameters in Bradley et al. (2016), as shown in Fig. 6. Most paleo-MSL points during 8–6 ka in the study area were included in the range, with ICE-5G in the study area model as the upper limit and Model A in the Gunsan Bay model as the lower limit (Fig. 6). However, the paleo-MSL points observed after 6 ka were distributed above and below the Model A curve of the Gunsan Bay model.

Comparing the slopes from the predicted paleo-MSL models of Bohai Bay, Tando Estuary, and Gunsan Bay up to ~7 ka, indicated steeper slopes from Bohai Bay in the north to Gochang-Yeonggwang in the south of the Yellow Sea, approaching the slope of the glacio-eustatic sea-level curve (green curve in Fig. 6). However, because the Gunsan model was based on the tectonic and structural characteristics of the South China Sea or Malay Peninsula (Bradley et al., 2016), it could be employed to support these proposals. It can be assumed, therefore, that the levering effect of the transgression in the early Holocene decreased southward in the Yellow Sea (Fig. 6).

5.4. Comparison of sea-level changes in the study area and eastern part of the South Sea of the Korean Peninsula

Based on the indicative paleo-MSL shown in Table 4, the R package ggplot2 software was employed to plot the RSL curve in the study area. The red line and shaded area represent the loess smooth curve (span 0.3) and 95% confidence interval (Fig. 7). As the figure indicates, the indicative paleo-MSL point and RSL curve of the survey area are shown together, along with the MSL curve for Gunsan Bay. In addition, to compare the RSL of the study area with that of the South Sea, the RSLs of the Bibong site (Hwang et al., 2013) in the reaches of the lower Nakdong River and Gwanpo Port on Geoje Island were plotted together. The RSL curve of the study site was compared with that of the Toyo-oka Basin (Tanigawa et al., 2013) on the west coast of Japan. The slope of the RSL curve of the study area was steepest at ~8 ka on the east coast of the Yellow Sea, but it was generally lower than that of Gunsan Bay, except in the 8–7 ka section. As discussed in the previous section, the steep early Holocene slope and low highstand of the RSL curve indicated minimal levering effect on the east coast of the Yellow Sea. Moreover, the sea-level changes were estimated to have been influenced by glacio-eustatic sea-level changes, such as a slight decrease at 3 ka and a subsequent increase after 2 ka.

As discussed previously, the levering effect of the early Holocene transgression on the east coast of the Yellow Sea caused regional differences in the impact of the tectonic structure. As observed in several GIA models, the levering effect appeared at ~6 ka in the mid-Holocene and declined significantly toward the late Holocene. However, as variations in paleo-MSL appeared during the late Holocene, we compared the study site data with those from the east coast of the South Sea. The paleo-MSL points are connected by blue dotted lines, as shown in Fig. 7. The bottom part of the red line represents the paleo-MSL points of GP03, and the upper part those of GP01. The paleo-MSL points of GP01 were higher than those of GP03 (Fig. 7, Table 4). This phenomenon could be considered an instance of the paleo-MSL being recorded under the influence of the topography, even within a single salt marsh. In addition, the paleo-MSL could be affected by erosion and redeposition in the channel form, as in the Tando Estuary (Yang et al., 2022). In conclusion, the slight fluctuation range of the paleo-MSL data in the late Holocene in the study area could be ascribed to the formation of event layers in the

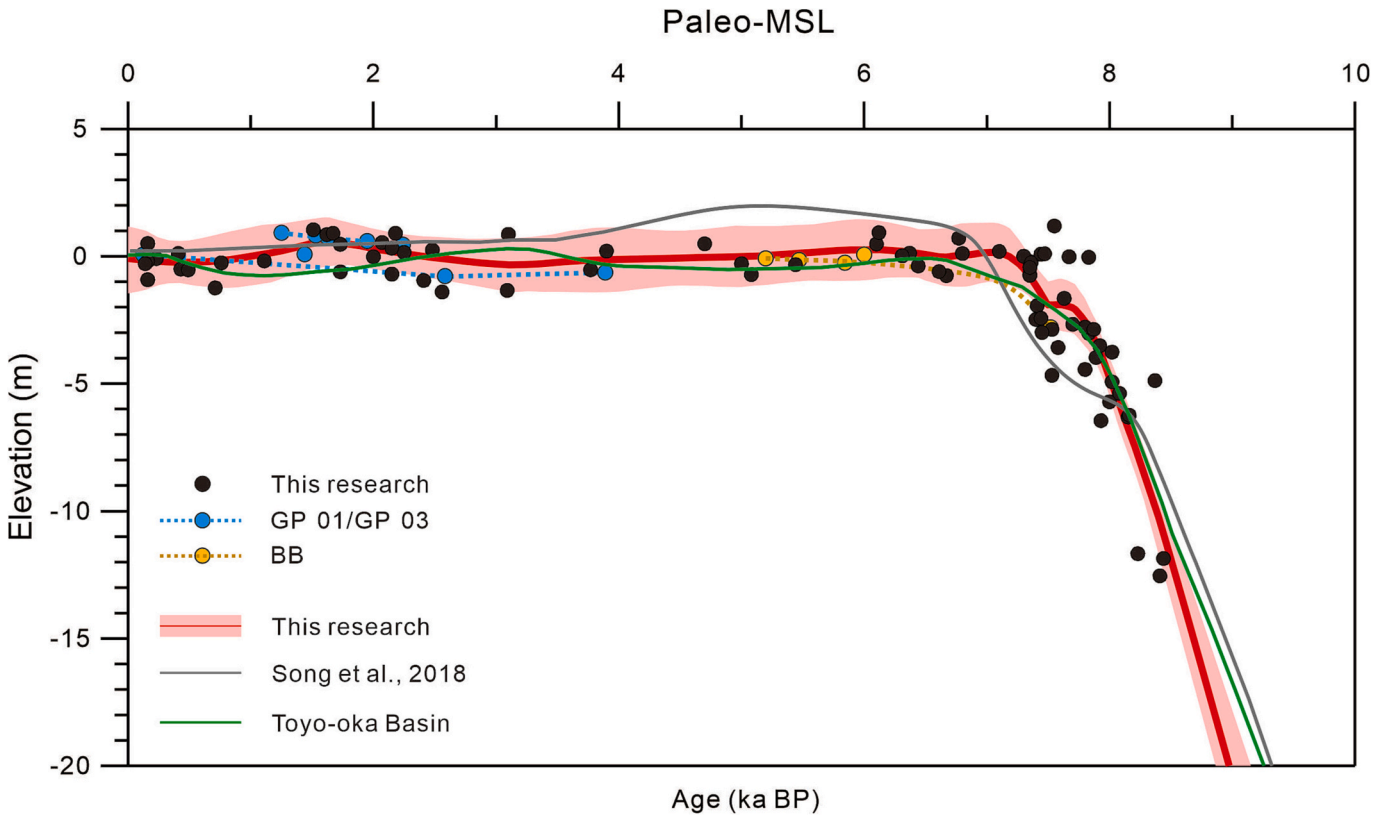

Fig. 7. Relative sea level change curves (red line) and observed paleo-mean-sea-level (paleo-MSL) points (black circles) in the study area. The curve of the study area was compared with those of Gunsan Bay (Song et al., 2018), Gwanpo Port, Bibong and Toyo-oka Basin (Tanigawa et al., 2013). Before 8 ka, the slope of the sea level curve in the study area was steepest but, subsequently, the highstand in Gunsan Bay was higher than at the study site. During the late Holocene, all curves fall within the buffer zone of the study site, but each curve shows a slightly different pattern. (For interpretation of the references to colour in this figure legend, the reader is referred to the web version of this article.)

coastal land, erosion and redeposition in the channel, and topographical effects.

However, based on the scattering of shell layers and diatom evidence, the Bibong archeological site in the lower reaches of the Nakdong River appears to have been a coastal area or salt marsh affected by the sea during the middle Holocene (Hwang et al., 2013). The paleo-MSL was estimated using data from Hwang et al. (2013), as shown in Table 4 and Figs. 6 and 7. As shown in Fig. 7, the paleo-MSLs were − 2.8 m at 7.53 ka and − 0.27–0.05 m during 5.2–6.01 ka, almost identical to the current MSL (−0.27 m, Table 2). Because the Bibong area is approximately 70 km from the Nakdong Estuary, transgression caused no levering effect in the early Holocene, apparently reflecting only the paleo-MSL at that time. The RSL curve of the Bibong site in the mid-Holocene is similar to that of Toyo-oka Basin, western Japan (Tanigawa et al., 2013). However, the RSL curves of the study area and Toyo-oka Basin show contrasting changes in the late Holocene (Fig. 7), although these are within the error range on the RSL curve of the study site. The late Holocene sea-level change of the study site was estimated to have been influenced by glacio-eustatic sea-level change, such as a slight decrease at 3 ka and subsequent rise after 2 ka.

6. Conclusions

The Holocene RSL of the Gochang-Yeonggwang site was compared with that at Bohai Bay, Tando Estuary, and Gunsan Bay in the Yellow Sea, the east coast of the South Sea, and the Toyo-oka Basin on the west coast of Japan. A multi-proxy approach, including lithostratigraphy combined with radiocarbon dating and analyses of grain size distribution, magnetic susceptibility, and geochemistry facilitated the generation of 89 paleo-sea-level points reconstructed from 28 borehole sediments.

The early Holocene transgression in the study site (−11.86 m elevation at 8.44 ka) started later and on a shallower layer than those of Gunsan Bay (−27.9 m at 9.8 ka), although the two regions are only 150 km apart. These conclusions were inferred from the substantial differences in sediment inflow evidenced by the size of the river basin, pre-Holocene topography, and tectonic characteristics. Comparing the slopes and highstands from the predicted paleo-MSL models of Bohai Bay, Tando Estuary, and the study site up to ~7 ka, the slopes and highstands were steeper and lower, respectively, from Bohai Bay in the north to the Gochang-Yeonggwang area in the south of the Yellow Sea, approaching the slope of the glacio-eustatic sea-level curve. It could be assumed that the levering effect of transgression in the early Holocene decreased southward in the Yellow Sea. The slight fluctuation in the paleo-MSL points of the late Holocene in the study area could be ascribed to the formation of event layers in the coastal land, erosion and redeposition in the channel, and topographical effects. However, the sea-level changes in the late Holocene were influenced by glacio-eustatic sea-level changes, such as a slight decrease at 3 ka and a subsequent increase after 2 ka.

Declaration of Competing Interest

None.

Data availability

Data will be made available on request.

Acknowledgment

This work was supported by the Basic Research Project (GP2022-006) of the Korea Institute of Geoscience and Mineral Resource (KIGAM), Korean Ministry of Science and ICT.

Appendix A. Supplementary data

Supplementary data to this article can be found online at https://doi.org/10.1016/j.palaeo.2023.111779.

References

Amante, C., Eakins, B.W., 2009. ETOPO1 Global Relief Model Converted to PanMap Layer Format. NOAA National Geophysical Data Center. PANGAEA. https://doi.org/10.1594/PANGAEA.769615.

Bak, Y.S., 2015. Mid-Holocene Sea-level fluctuation inferred from diatom analysis from sediments on the west coast of Korea. Quat. Int. 384, 139–144. https://doi.org/10.1016/j.quaint.2014.08.018.

Bloom, A.L., Park, Y.A., 1985. Holocene Sea-level history and tectonic movements, Republic of Korea. Quat. Res. 24, 77–84. https://doi.org/10.4116/jaqua.24.77.

Blott, S.J., Pye, K., 2001. GRADISTAT: a grain size distribution and statistics package for the analysis of unconsolidated sediments. Earth Surf. Process. Landf. 26, 1237–1248. https://doi.org/10.1002/esp.261.

Bradley, S.L., Milne, G.A., Horton, B.P., Zong, Y., 2016. Modelling Sea level data from China and Malay-Thailand to estimate Holocene ice-volume equivalent sea level change. Quat. Sci. Rev. 137, 54–68. https://doi.org/10.1016/j.quascirev.2016.02.002.

Byun, D.S., Choi, B.J., Kim, H., 2019. Estimation of the lowest and highest astronomical tides along the west and south coast of Korea from 1999 to 2017. J. Korean Soc. Oceanogr. 24, 495–508. https://doi.org/10.7850/jkso.2019.24.4.495.

Chagué-Goff, C., 2010. Chemical signatures of palaeotsunamis: a forgotten proxy? Mar. Geol. 271, 67–71. https://doi.org/10.1016/j.margeo.2010.01.010.

Chang, J.H., Choi, J.Y., 2001. Tidal-flat sequence controlled by Holocene Sea-Level rise in Gomso Bay, West Coast of Korea. Estuar. Coast. Shelf Sci. 52, 391–399. https://doi.org/10.1006/ecss.2000.0745.

Chang, J.H., Park, Y.A., Han, S.J., 1996. Late Quaternary stratigraphy and sea-level change in the tidal flat of Gomso Bay, west coast of Korea. J. Korean Soc. Oceanogr. 1, 59–72.

Chough, S.K., Lee, H.J., Yoon, S.H., 2000. Marine Geology of Korean Seas. In: Elsevier, Amsterdam, p. 313 pp..

Chun, S.S., Yang, B.C., 2004. Sedimentation and Holocene evolution of wave dominated, macrotidal-flat depositional system in the southwestern open coasts of Korean Peninsula. SedimentolSoc. Japan J. 58, 65–83. https://doi.org/10.4096/jssj1995.58.65.

Clark, J.A., Farrell, W.E., Peltier, W.R., 1978. Global changes in Postglacial Sea Level: a numerical calculation. Quat. Res. 9, 265–287. https://doi.org/10.1016/0033-5894(78)90033-9.

Costa, L.S., Huszar, V.L.M., Ovalle, A.R., 2009. Phytoplankton functional groups in a tropical estuary: Hydrological control and nutrient limitation. Estuar. Coasts 32, 508–521. https://doi.org/10.1007/s12237-009-9142-3.

Cummings, D.I., Dalrymple, R.W., Choi, K., Jin, J.H., 2015. The Tide-Dominated Han River Delta. Elsevier, Amsterdam, Korea. https://doi.org/10.1016/C2013-0-15362-7.

Cummings, D.I., Dalrymple, R.W., Choi, K., Jin, J.H., 2016. The Tide-Dominated Han River Delta. In: Korea, Amsterdam, Elsevier, p. 376.

Eakins, B.W., Sharman, G.F., 2012. In: Hypsographic Curve of Earth's Surface from ETOPO1, 5. NOAA National Geophysical Data Center, Boulder, CO, p. 1.

Fan, D., Wang, Y., Liu, M., 2013. Classifications, sedimentary features and facies associations of tidal flats. J. Palaeogeogr. 2, 66–80. https://doi.org/10.3724/SP.J.1261.2013.00018.

Farrell, W.E., Clark, J.A., 1976. On Postglacial Sea level. Geophys. J. Int. 46, 647–667. https://doi.org/10.1111/j.1365-246X.1976.tb01252.x.

Folk, R.L., Ward, W.C., 1957. A Study in the significance of Grain-size Parameters. J. Sediment. Petrol. 27, 3–26. https://doi.org/10.1306/74D70646-2B21-11D7-8648000102C1865D.

Hunt, M.W., Speakman, R.J., 2015. Portable XRF analysis of archaeological sediments and ceramics. J. Archaeol. Sci. 53, 626–638. https://doi.org/10.1016/j.jas.2014.11.031.

Hwang, S.I., Kim, J.Y., Yoon, S.O., 2013. Sea level Change during the middle Holocene at Bibong-ri, Changnyeong-gun, Gyeongsangnam-do, South Korea. J. Korean Geogr. Soc. 48, 837–855 (in Korean with English Abstract).

Jang, Y., Kwon, S., Yi, K.W., 2015. Structural style of the Okcheon fold-thrust belt in the Taebaeksan Zone, Korea. J. Asian Earth Sci. 105, 140–154. https://doi.org/10.1016/j.jseaes.2015.03.017.

Jung, T.S., 2014. Change of mean sea level due to coastal development and climate change in the Western Coast of Korean peninsula. J. Korean Soc Mar. Eng. 26, 120–130. https://doi.org/10.9765/KSCOE.2014.26.3.120 (in Korean with English abstract).

Kim, M.S., Chu, K.S., Kim, O.S., 1986. Investigation of some Influence of the Nakdong River Water on Marine Environment in the Estuarine Area using Landsat Imagery. Tech. Rep. Korea Min. Sci. Tech. 93–147 (in Korean with English abstract).

Kim, S.W., Oh, C.W., Ryu, I.C., William, I.S., Sajeev, K., Santosh, M., Rajesh, V.J., 2006. Neoproterozoic Bimodal Volcanism in the Okcheon Belt, South Korea, and its Comparison with the Nanhua Rift, South China: Implications for Rifting in Rodinia. J. Geol. 114, 717–733. https://doi.org/10.1086/507616.

Kim, Y.H., Lee, H.J., Chun, S.S., Han, S.J., Chough, S.K., 1999. Holocene transgressive stratigraphy of a macrotidal flat in the southeastern Yellow Sea: Gomso Bay,Korea. J. Sediment. Res. 69, 328–337. https://doi.org/10.2110/jsr.69.328 (in Korean with English abstract).

Koh, H.J., Ko, K., Kwon, C.W., Kee, W.S., Kim, B.C., Kim, S.W., Kim, Y.B., Khim, Y.H., Kim, H.C., Park, S.I., Song, K.Y., Yeon, Y.K., Lee, S.R., Lee, S.S., Lee, S.R., Lee, S.B., Lee, H.J., Cho, D.R., Chi, K.H., Choi, S.J., Choi, B.Y., Hwan, J.K., Hwang, J.H., Hyeon, H.J., Hong, B., Jeon, H.Y., Kim, Y.S., Roh, J.R., Kang, K.H., 2015. Tectonostratigraphy of the Mid-West Korean Peninsula and Construction of the Integrated Geoscience Information System. Basic Research Report of the Korea Institute of Geoscience and Mineral Resources, 243 pp.

Korea Hydrographic Office, 1982. http://www.khoa.go.kr/eng/kcom/cnt/selectContentsPage.do?cntId=11030000.

Korea Hydrographic and Oceanographic Administration, 2013. Tidal bench mark (http://sms.khoa.go.kr/koofs/tbm/tbm.asp?tl_id¼502, accessed 10 May 2015).

Korea Meteorological Administration, 2013–2014. https://web.kma.go.kr/eng/biz/act.jsp.

Korea Ocean Research and Development Institute, 1994. Quaternary Sea-Level Changes and Their Implication in the Evolution of Coastal Depositional Environments (III). Seoul, Korea, Korea Ocean Research and Development Institute, Report BSPN 00223–732-5, 315 pp.

Kwon, C.W., Ko, K., Koh, H.J., 2015. Geological Report of the Beopseongpo, Anmado, Songido, Bunamgundo, Imjado Sheets (1:50,000). In: Daejeon, Korea Institute of Geoscience and Mineral Resources, p. 57.

Lambeck, K., Smither, C., Johnston, P., 1998. Sea-level change, glacial rebound and mantle viscosity for northern Europe. Geophys. J. Int. 134, 102–144. https://doi.org/10.1046/j.1365-246x.1998.00541.x.

Lee, E., Chang, T.S., 2015. Holocene Sea level changes in the Eastern Yellow Sea: a brief review using proxy records and measurement data. J. Korean Earth Sci. Soc. 36, 520–532. https://doi.org/10.5467/JKESS.2015.36.6.520 (in Korean with English abstract).

Lim, D.I., Choi, J.Y., Jung, H.S., 2003. Characteristics and stratigraphy of late Quaternary sediments on a macrotidal mudflat deposit of Namyang Bay, western coast of Korea. J. Korean Earth Sci. Soc. 24, 46–60 (in Korean with English abstract).

Liu, F., Zhou, Y., 2019. Nd isotopic and model age study of the Shandong Province, North China Craton: Implications for correlation with South Korea. J. Earth Sci. 30, 938–951. https://doi.org/10.1007/s12583-019-1213-1.

Lowe, J.A., Bernie, D., Bett, P., Bricheno, L., Brown, S., Calvert, D., Clark, R., Eagle, K., Edwards, T., Fosser, G., Fung, F., Gohar, L., Good, P., Gregory, J., Harris, G., Howard, T., Kaye, N., Kendon, E., Krijnen, J., Maisey, P., McDonald, R., McInnes, R., McSweeney, C., Mitchell, J.F.B., Murphy, J., Palmer, M., Roberts, C., Rostron, J., Sexton, D., Thornton, H., Tinker, J., Tucker, S., Yamazaki, K., Belcher, S., 2018. UKCP18 Science Overview Report, 73p.

Meijles, E.W., Kiden, P., Streurman, H.J., van der Plicht, J., Vos, P.C., Gehrels, W.R., Kopp, R.E., 2018. Holocene relative mean sea-level changes in the Wadden Sea area, northern Netherlands. J. Quat. Sci. 33, 905–923. https://doi.org/10.1002/jqs.3068.

National Geographic Institute, 1983. Basic map of nearshore of Korea (1:25000, map No. NI52-1-16-4, Beopseong-po).

National Geographic Institute, 1996. Basic map of nearshore of Korea (1:25000, map No. NI52-6-07-3, Geoje).

Oh, I.S., Lee, D.E., 1998. Tides and tidal currents of the Yellow and East China Seas during the last 13000 years. J. Korea Soc. Oceanogr. 33, 137–145 (in Korean with English abstract).

Oh, K.C., Kim, J.Y., Yang, D.Y., Hong, S.S., Lee, J.Y., Lim, J., 2010. Origin, age and sedimentation rate of Mid-Geum. Econ. Environ. Geol. 43, 333–341 (in Korean with English abstract).

Park, S.C., Chu, K.S., 1991. Dispersal patterns of River-Derived Fine-Grained Sediments on the Inner Shelf of Korea Strait. Elsevier Oceanogr. Ser. 54, 231–240. https://doi.org/10.1016/S0422-9894(08)70098-9.

Park, J.M., Kim, S.W., Park, S.H., 2007. In: Study on Growth Characteristics of Piuns thunbergii Windbreak Forests around Goosipo Beach, Gochang-Gun, fall academic presentation, pp. 108–111 (in Korean with English abstract).

Peltier, W.R., 2004. Global glacial isostasy and the surface of the ICE-age Earth: the ICE-5G (VM2) model and GRACE. Annu. Rev. Earth Planet. Sci. 32, 111–149. https://doi.org/10.1146/annurev.earth.32.082503.144359.

Peltier, W.R., Tushingham, A.M., 1989. Global Sea level rise and the greenhouse effect: might they be connected? Science 244, 806–810. https://doi.org/10.1126/science.244.4906.806.

Peltier, W.R., Argus, D.F., Drummond, R., 2015. Space geodesy constrains ICE age terminal deglaciation: the global ICE-6G_C (VM5a) model. J. Geophys. Res. Solid Earth 120, 450–487. https://doi.org/10.1002/2014JB011176.

Radu, T., Diamond, D., 2009. Comparison of soil pollutions determined using AAS and portable XRF techniques. J. Hazard. Mater. 171, 1168–1171. https://doi.org/10.1016/j.jhazmat.2009.06.062.

Ramsey, C.B., 2017. Methods for summarizing radiocarbon datasets. Radiocarbon 59, 1809–1833. https://doi.org/10.1017/RDC.2017.108.

Reimer, P.J., Bard, E., Bayliss, A., Beck, J.W., Blackwell, P.G., Ramsey, C.B., Buck, C.E., Cheng, H., Edwards, R.L., Friedrich, R.M., Grootes, P.M., Guilderson, T.P., Haflidason, H., Hajdas, I., Hatte, C., Heaton, T.J., Hoffmann, D.L., Hogg, A.G., Hughen, K.A., Kaiser, K.F., Kromer, B., Manning, S.W., Niu, M., Reimer, R.W., Richards, D.A., Scott, E.M., Southon, J.R., Staff, R.A., Turney, C.S.M., van der Plicht, J., 2013. Intcal13 and Marine13 radiocarbon age calibration curves 0–50,000 years cal BP. Radiocarbon 55, 1869–1887. https://doi.org/10.2458/azu_js_rc.55.16947.

Roy, K., Peltier, W.R., 2018. Relative Sea level in the Western Mediterranean basin: a regional test of the ICE-7G_NA (VM7) model and a constraint on late Holocene Antarctic deglaciation. Quat. Sci. Rev. 183, 76–87. https://doi.org/10.1016/j.quascirev.2017.12.021.

Simpson, M.J.R., Ravndal, O.R., Sande, H., Nilsen, J.E.Ø., Kierulf, H.P., Vestøl, O., Steffen, H., 2017. Projected 21st century sea-level changes, observed sea level extremes, and sea level allowances for Norway. J. Mar. Sci. Eng. 5, 36. https://doi.org/10.3390/jmse5030036.

Song, B., Yi, S., Yu, S.Y., Nahm, W.H., Lee, J.Y., Lim, J., Kim, J.C., Yang, Z., Han, M., Jo, K.N., Saito, Y., 2018. Holocene relative sea-level changes inferred from multiple proxies on the west coast of South Korea. Palaeogeogr. Palaeoclimatol. Palaeoecol. 496, 268–281. https://doi.org/10.1016/j.palaeo.2018.01.044.

Spada, G., Melini, D., 2019. SELEN4 (SELEN version 4.0): a Fortran program for solving the gravitationally and topographically self-consistent sea-level equation in glacial isostatic adjustment modeling. Geosci. Model Dev. 12, 5055–5075. https://doi.org/10.5194/gmd-12-5055-2019.

Tanigawa, K., Hyodo, M., Sato, H., 2013. Holocene relative sea-level change and rate of sea-level rise from coastal deposits in the Toyooka Basin, western Japan. The Holocene 23, 1039–1051. https://doi.org/10.1177/0959683613479680.

Tegmark, M., 1996. An Icosahedron-based method for pixelizing the celestial sphere. Astrophys. J. 470, L81–L84. https://doi.org/10.1086/310310.

Vink, A., Steffen, H., Reinhardt, L., Kaufmann, G., 2008. Holocene relative sea-level change, isostatic subsidence and the radial viscosity structure of the mantle of Northwest Europe (Belgium, the Netherlands, Germany, southern North Sea). Quat. Sci. Rev. 26, 3249–3275. https://doi.org/10.1016/j.quascirev.2007.07.014.

Wang, Z., Zhan, Q., Long, H., Saito, Y., Gao, X., Wu, X., Li, L., Zhao, Y., 2013. Early to mid-Holocene rapid sea-level rise and coastal response on the southern Yangtze delta plain,China. J. Quat. Sci. 28, 659–672. https://doi.org/10.1002/jqs.2662.

Wang, F., Zong, Y., Mauz, B., Li, J., Fang, J., Tian, L., Chen, Y., Shang, Z., Jiang, X., Spada, G., Melini, D., 2020. Holocene Sea-level change on the central coast of Bohai Bay,China. Earth Surf. Dyn. 8, 679–693. https://doi.org/10.5194/esurf-8-679-2020.

Watson, P.J., Lim, H.S., 2020. An update on the status of mean sea level rise around the Korean Peninsula. Atmos. 11, 1153. https://doi.org/10.3390/atmos11111153.

Yang, B.C., Chun, S.S., 2001. A seasonal model of surface sedimentation on the Baeksu open-coast intertidal flat, southwestern coast of Korea. Geosci. J. 5, 251–262. https://doi.org/10.1007/BF02910308.

Yang, B.C., Dalrymple, R.W., Chun, S.S., 2005. Sedimentation on a wave-dominated, open-coast tidal flat, southwestern Korea: Summer tidal flat – winter shoreface. Sedimentology 52, 235–252. https://doi.org/10.1111/j.1365-3091.2004.00692.x.

Yang, D.-Y., Han, M., Kim, J.C., Lim, J., Yi, S., Kim, J.-Y., 2016. Characteristics of marine terrace sediments formed during the marine isotope stage 5e in the west south coast of the Korean Peninsula. Eco. Env. Geol. 49, 417–432. https://doi.org/10.9719/EEG.2016.49.6.417 (in Korean with English abstract).

Yang, D.Y., Han, M., Yoon, H.H., Cho, A., Kim, J.C., Choi, E., Kashima, K., 2022. Early Holocene relative sea-level changes on the central east coast of the Yellow Sea. Palaeogeogr. Palaeoclimatol. Palaeoecol. 603, 111185 https://doi.org/10.1016/j.palaeo.2022.111185.

Yokoyama, Y., Purcell, A., 2021. On the geophysical processes impacting palaeo-sea-level observations. Geosci. Lett. 8, 13. https://doi.org/10.1186/s40562-021-00184-w.

Yoon, H.H., Ryang, W.H., Chun, S.S., Alexander, R.S., Kim, J.C., Chang, T.S., Yoo, D.K., Hong, S.H., 2023. Coastal switching of dominant depositional processes driven by decreasing rates of Holocene Sea-level rise along the macro tidal coast of Gochang, SW Korea. J. Sediment. Res. 93, 20–36. https://doi.org/10.2110/jsr.2021.023.